Assessment of Noise Reduction Concepts for Leading-Edge Slat Noise

Yang Zhang* and Adam O'Neill† and Louis N. Cattafesta III‡
Florida Center for Advanced Aero-Propulsion (FCAAP), Florida A&M University and Florida State University, Tallahassee, Florida, 32310

Kyle Pascioni§
National Institute of Aerospace, Hampton, VA, 23666

Meelan M. Choudhari¶ and Mehdi R. Khorrami‖ and David P. Lockard** and Travis Turner††
NASA Langley Research Center, Hampton, VA, 23681

The leading-edge slat of a high-lift airfoil can be a significant noise contributor during aircraft landing. This paper summarizes the effects of several passive noise reduction devices on the 30P30N high-lift airfoil. Experiments are conducted on a two-dimensional multi-element high-lift airfoil with leading-edge slat extensions, gap filler, and cove filler in an anechoic wind tunnel to evaluate the effect of passive flow control on the acoustics generated by the unsteady flow field. Slat geometry modifications associated with the treatments alter the flow field in the region that dominates the generation of the acoustic field. Three angles of attack ($\alpha_k = 8°$, $10°$, and $15.5°$) and three different Reynolds numbers ($Re_c = 1.2e6$, $1.5e6$, and $1.71e6$) are selected as the test conditions. Steady surface pressure measurements are conducted to assess the effect of the treatments on the lift and drag. Unsteady surface pressure measurements along with the far-field acoustic array measurements are performed to evaluate the changes in near- and far-field pressure fluctuations, respectively. Delay and Sum (DAS) beamforming method is applied to locate the noise sources on the model and provide integrated spectra. Implementation difficulties with the gap filler led to structural integration deficiencies that prevented a fair assessment of this technology. Among the other passive devices, the cove filler shows the most effective noise reduction, along with a negligible change in the aerodynamic metrics.

I. Introduction

Along with the landing gear, a deployed high-lift system contributes a significant portion of the radiated noise from an aircraft during approach. The leading-edge slat is often the dominant noise contributor associated with the wing. While the flap side edges can be more intense sources of noise, the noise source associated with the slat is distributed over a larger region, and hence, can result in a larger contribution to the far field noise upon integration over the source region [1].

Slat noise is composed of several flow-induced source mechanisms. Time-accurate numerical simulations have shown ample evidence that slat trailing edge shedding produces a high Strouhal number spectral peak ($20 < St_s < 40$, where the characteristic length scale s is based on the slat chord) [2, 3]. In addition, strong narrow-band peaks in the mid-Strouhal range ($1 < St_s < 5$) are observed in both the near field surface pressure spectra and far field spectra in experiments, and have been linked to a flow-acoustic feedback of slat cove shear layer instabilities [4, 5]. This phenomenon is analogous to Rossiter modes [6] in the context of open cavity flows. Also, recent experiments suggest the existence of an additional, low-Strouhal number peak ($St_s \approx 0.15$) [5] due to bulk cove oscillation. Phase-locked

*Postdoctoral scholar, Department of Mechanical Engineering, AIAA Member. yz12b@my.fsu.edu
†Graduate research assistant, Department of Mechanical Engineering, AIAA Student Member.
‡Professor and University Eminent Scholar, Department of Mechanical Engineering, AIAA Associate Fellow.
§Postdoctoral research scholar, AIAA member.
¶Aerospace Technologist, AIAA Associate Fellow.
‖Aerospace Technologist, AIAA Associate Fellow.
**Aerospace Technologist, AIAA Senior Member.
††Aerospace Technologist, AIAA Senior Member.

PIV measurements display large-scale structures in the recirculation region. This cove oscillation is related to the unsteadiness of shear layer impingement location on the concave side, which is indicative of shear-layer flapping. Slat noise is also known to have a broadband component with a peak in the Strouhal range close to unity. Choudhari and Khorrami[7] attribute this to unsteady vortical structures produced by the cove shear layer interacting with the airfoil surfaces. This idea is corroborated by Knacke and Thiele [8], who used statistical correlation techniques to provide evidence that the principal source of the noise is due to unsteady structures interacting with the slat trailing edge.

Given the basic knowledge of the slat flow field, a variety of noise reduction techniques have been studied. The aim is to either reduce the region of flow unsteadiness or alter their position such that they minimally interact with the airfoil surfaces. The most common technique is designed to fill the cove such that flow separation is minimized or completely removed. In essence, a cove filler is attached to the slat with a shape bounded by the slat underside and the shear layer path, resulting in a streamlined slat. Choudhari et al.[9] found that broadband noise decreases between 0-20 kHz, where cove noise is prominent. Streett et al.[10] also found reduction in overall levels, but noted little or even adverse effects when changing the angle of attack. This indicates that deviations in shear layer path at off-design conditions are likely to limit the effectiveness of a given cove filler geometry to a narrow range of angles of attack. Imamura et al.[11] also found noise reduction due to cover filler at low frequencies, but the source levels increased for the spectral peak associated with trailing edge shedding. It appears that the streamlined geometry of the slat with a cove filler allows for more orderly vortex shedding of the slat wake, resulting in a stronger noise source at high frequencies.

Turner et al.[12] proposed using a deformable skin element to close the gap between the slat trailing edge and main wing leading edge. The gap filler device is expected to reduce noise by eliminating the interactions between slat cove unsteady structures and the slat trailing edge and slat gap regions. However, the noise reduction potential of this device has not been evaluated until now. Chevrons have also been introduced at the cusp to enhance mixing of the shear layer, an idea that has been successfully employed to reduce jet noise [13]. Kopiev et al.[14] performed a parametric study of different heights and angles of the serrations, finding an optimal geometry definition. However, some serration geometries were found to increase both narrow-band and broadband levels, indicating a complex dependence of the flow field on the serration parameters. An in-depth, physics-based study needs to be performed to determine the best set of geometric parameters before chevrons can be applied in a reliable manner. Other studies include the use of acoustic liners [15] and dielectric barrier discharge (DBD) actuators [16]. All of these techniques show potential merit but are relatively understudied. Great care must be taken to not affect the aerodynamic performance, because the flow field can be very sensitive to small changes. Spaid [17] demonstrates element wake merging to be crucial to the maximum lift capability. Hence, losses in performance may accrue if flow control is applied to a high-lift system that has already been optimized aerodynamically.

This paper documents the relative noise reduction characteristics of several passive control treatments on a common flow field. Specifically, a cove filler, a slat/main element gap filler, and slat cusp extensions with different lengths are implemented on the 30P30N two-dimensional airfoil. Each treatment is applied individually, and steady and fluctuating surface pressure and acoustic measurements are used to assess their effects.

II. Experimental Setup

A. Wind tunnel facility and airfoil model

The experiments were conducted in the Florida State Aeroacoustic Tunnel (FSAT) facility located at the Florida Center for Advanced Aero-Propulsion (FCAAP) at the Florida State University (FSU) [18]. The wind tunnel facility can be operated in either an open-jet or closed configuration. All of the tests in the current work were carried out in the closed test section with two Kevlar panels. The test section has dimensions of 2.74 m (L) by 1.22 m (W) by 0.91 m (H) in the streamwise, spanwise, and vertical directions, respectively. The two-dimensional airfoil model is mounted vertically, spanning the full height in the middle of the test section, with a schematic and primary dimensions provided in Figure 1 and Table 1, respectively. The total pressure is measured using a Pitot probe approximately 0.9 m upstream of the airfoil. The static pressure tap is on the contraction floor farther upstream to avoid blockage effects due to the model, and a correction is applied based on the area ratio. Combinations of three angles of attack (α_k = 8°, 10°, and 15.5°) and three chord-based Reynolds numbers (Re_c = 1.2e6, 1.5e6, and 1.71e6) with corresponding Mach numbers of 0.12, 0.15, and 0.17, respectively, are selected as the test conditions in the current study. For details of the test article, model rigging parameters, and the surface mounted instrumentation, the reader is directed to the Choudhari and Lockard [19], who provide an overview of the computational predictions and measurement data contributed to Category 7 of the 3rd AIAA Workshop on Benchmark Problems for Airframe Noise Computations (BANC-III), which

was held in Atlanta, GA, on June 14-15, 2014. As described by them, the geometry of the slat used in the BANC series of workshops as well as during the present effort involves minor modifications to the slat contour from the original 30P30N configuration. It should be noted that the angles of attack used here are the physical angle measured inside the test section. As mentioned in [20], these angles correspond to effective free-air AOA of 5.5°, 7.5°, and 9.5° based on comparisons with steady, Reynolds averaged Navier-Stokes computations with the Spalart-Allmaras turbulence model. There are two coordinate systems used in the current work. For keeping the location of pressure taps consistent at different AOA, the coordinates used in the C_p plots are fixed on the airfoil with the origin at the leading edge of the stowed airfoil, the x-direction along the chord, and the y-direction in the airfoil spanwise direction. For comparing the DAS source maps, the coordinate system origin is located at the middle of the test section (0.5c with respect to the first origin) with the x-direction along the flow direction, and the y-direction in the spanwise direction.

Several metal treatments are designed to alter the flow fields around the slat, including a slat cusp extension, a gap filler, and a cove filler. Each treatment is machined as three identical segments, each with a spanwise length of 12 inches. The stainless steel slat cusp extension is designed to delay the formation of the shear layer and shorten its trajectory path, which will likely result in reduced unsteadiness in the flow. The use of slat-cusp extensions as a noise reduction device is motivated by the previous calculations of Khorrami and Lockard [21] about the effects of a blade seal on noise radiation from the slat. Three extensions are tested and named *Ext1*, *Ext2*, and *Ext3*, respectively. A schematic and photographs of those three slat extensions are shown in Figure 2. The extension lengths measured from the slat cusp are l = 8.4 mm, 12.5 mm, and 16.3 mm, respectively. A total number of 18 rounded head screws (≈ 1.5mm thickness) are used to mount the slat extensions and thin masking tape is applied between the extension and the slat cove for sealing.

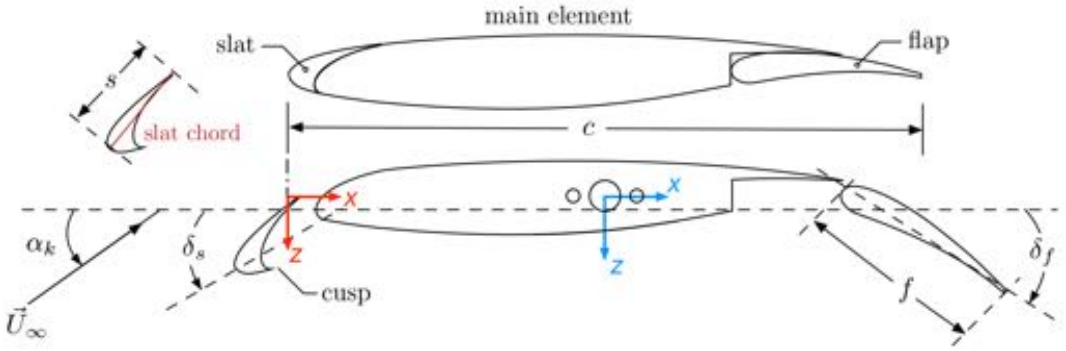

Fig. 1 Schematic of the 30P30N multi-element airfoil. The red coordinate is used for showing Cp distributions, and the blue coordinate is used for DAS beamforming source maps.

Table 1 Primary dimensions of 30P30N airfoil.

Stowed chord	c	0.457 m
Span length	b	0.914 m
Slat chord	s	0.15c
Flap chord	f	0.3c
Slat deflection angle	δ_s	30°
Flap deflection angle	δ_f	30°

The gap filler blocks the flow path across the slat gap within the original model, and hence, should eliminate the acoustic scattering of slat cove unsteadiness near the slat trailing edge and within the gap region. A more streamlined shape than that in Figure 3 would have been desirable to allow the flow over the suction surface of the slat to transition over the main wing. However, the slat rigging parameters of the 30P30N model, combined with geometric constraints on the attachment location over the main wing leading edge prevented the use of a highly streamlined shape during the present campaign, and furthermore, no priori computations were feasible to assess the performance of the gap filler design prior to its fabrication. Previous work has shown that most practical gap filler implementations involve mounting or deploying the gap filler from the main wing. However, in order to avoid making any modifications to the main wing, the gap filler was mounted to the slat in the present study, with the understanding that the measured performance of the

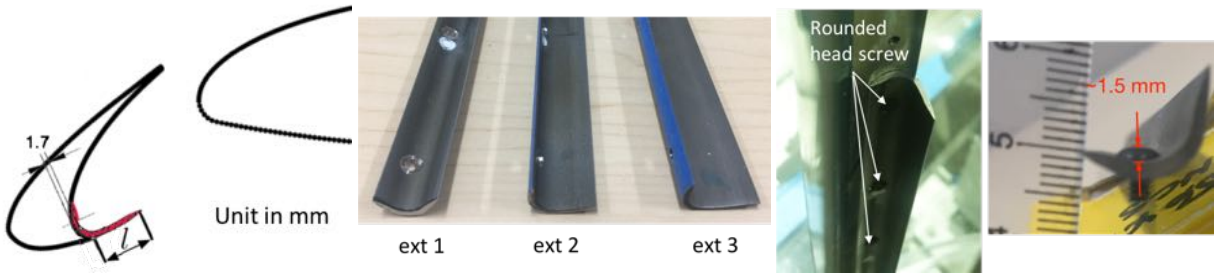

(a) Schematic **(b) Three extensions** **(c) Installation**

Fig. 2 Schematic and pictures of slat cusp extension.

suboptimal gap filler could be viewed as providing a lower bound on the effectiveness of this concept. Before directly mounting the gap filler to the slat, some minor adjustments were made as shown in Figure 3. Thin masking tape was applied between the gap filler and the slat cove to reduce the gap due to machining tolerance. A total number of 18 rounded head screws are used to reduce the intrusive effects on the flow field for mounting the gap filler. As can be seen from the suction side of the airfoil, there is a tiny gap between the gap filler and the main element, which is also due to machining tolerance. This gap was known to be undesirable, so measures to seal it were pursued. Efforts to seal this gap using silicone proved fruitless during testing. It is possible that this limitation had a negative effect on the assessment of the gap filler case, as will be discussed in greater detail in the results section.

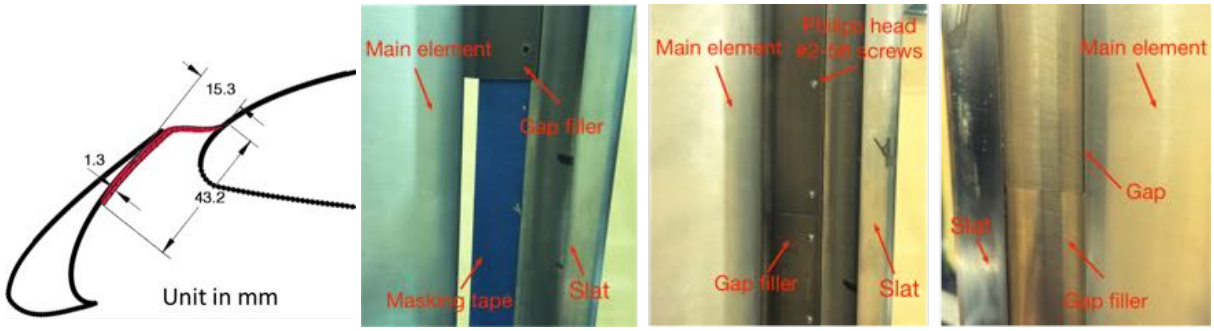

(a) Schematic **(b) Installation**

Fig. 3 Schematic and pictures of gap filler.

A schematic of the cove filler is shown in Figure 4a. The geometry is designed to have a streamline profile that was designed on the basis of computed, time averaged flow field within the slat cove region at a free-air angle of attack equal to 5.5° (equivalent to $\alpha_k = 8°$). It should be noted that the cove filler does not extend all the way to the slat trailing edge, but terminates in the vicinity of the mean reattachment location. Time accurate simulations [22] had confirmed the effectiveness of this cove filler design in reducing the slat noise by minimizing the extent of flow separation within the cove region. Each spanwise piece of the cove filler is aligned by two dowel pins, and machining holes are filled and smoothed using silicone. Theoretically, with the cove filler, the shear layer reattachment and feedback mechanism will be totally eliminated. Thus, the noise levels should be reduced. Because the cove filler is designed as an attachment and the slat cusp has a nominal thickness of 0.4mm, a smooth transition cannot be achieved at the joint, resulting in a small step as shown in Figure 4b. During the experiments, some anomalous noise peaks appeared in the pressure spectra, and the results are thus sensitive to the treatment on the surface near the joint as shown in Figure 5. This will be discussed in detail in the results section.

(a) Schematic (b) Installation

Fig. 4 Schematic and pictures of cove filler.

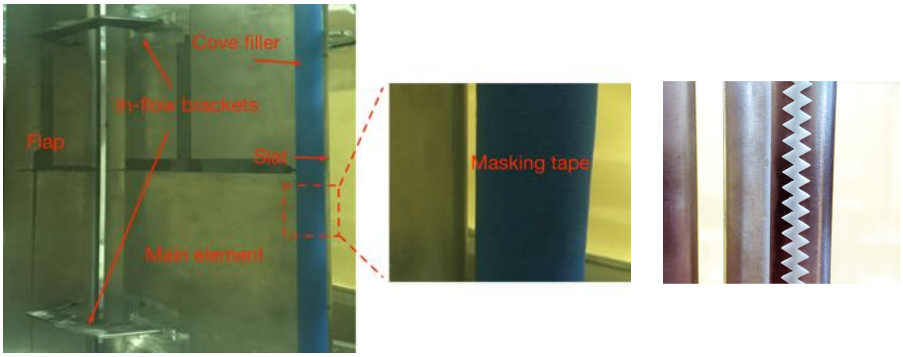

(a) Masking tape (b) BL trip

Fig. 5 Surface treatment applied in the cove filler case.

B. Steady surface pressure

Steady surface pressure is measured to characterize the aerodynamic performance, including lift and pressure drag for the airfoil. A total number of 122 static pressure ports are instrumented on the 30P30N model, distributed along the center and across the span at various locations as shown in Figure 6. For a given test condition, one hundred samples are acquired at 2 Hz for each channel and averaged to calculate the coefficient of pressure, $C_p = (p - p_\infty)/q_\infty$, at each location.

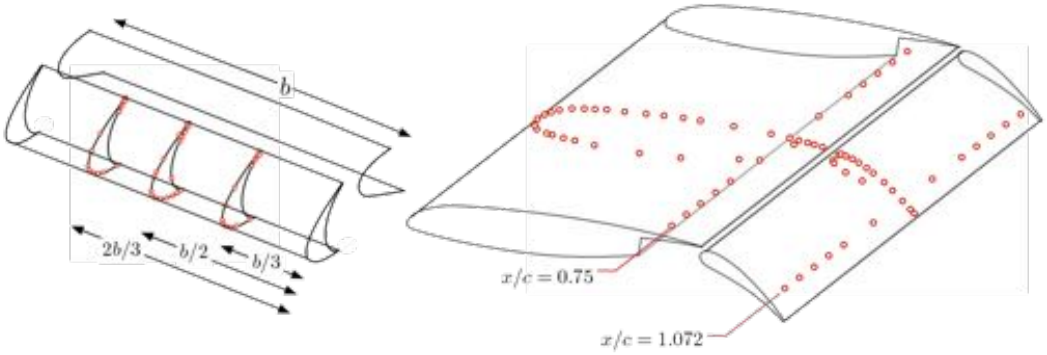

Fig. 6 Location of steady pressure taps on the 30P30N airfoil surface [23].

Once the steady pressure distribution is obtained, the lift coefficient is estimated by using the steady pressure distribution along the centerline [24]. The estimated lift coefficient as a function of the angle of attack α of the chord is then determined.

C. Unsteady surface pressure

Kulite unsteady pressure sensors are flush mounted on the slat to measure the local fluctuating pressure at different locations as shown in Table 2. During the measurements, the sensors are simultaneously sampled at 204.8 kHz for 30 seconds for each Kulite using a NI PXI 1045 chassis and ac-coupled NI 4498 cards (24-bit). Welch's method is applied to calculate frequency spectra using 16384 samples for the FFT with a Hanning window and 75% overlap across adjacent blocks, resulting in a bin resolution of 12.5 Hz and random uncertainty of 3.6% in Pa^2/Hz. It should be noted that the Kulite probe locations P_3, P_4, and P_5 are covered by the cove filler, and P_4 and P_5 are covered by the gap filler. Therefore, the spectra at these locations for these two treatments cannot be obtained.

Table 2 Locations of Kulite surface pressure sensors.

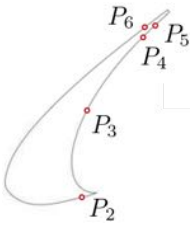

	x/c	y/b	z/c
P_2	-0.0379	-0.0346	0.1119
P_3	-0.0336	-0.0346	0.0578
P_4	0.0058	-0.0346	0.0070
P_5	0.0115	-0.0346	0.0017
P_6	0.0067	-0.0346	0.0020

D. Far-field acoustics

A phased microphone array contains a combination of 55 1/4-inch G.R.A.S. 40BE and Brüel and Kjær 4958 free field microphones to measure the far field acoustics for beamforming. The microphone layout was optimized through the use of Point Spread Function (PSF) simulations and monitoring its properties [25]. Phased array geometry has progressed from linearly spaced square grids to periodic patterns, for example, the log-spiral pattern shown in Figure 7. The frame that holds the microphones is designed to minimize acoustic reflections. It is an aluminum skeleton frame cut by a waterjet process and it is covered by 76 mm foam wedges. Each microphone is held away from the aluminum frame

by a 0.15 m long steel rod away from the aluminum frame to minimize acoustic reflections and near field scattering effects [23].

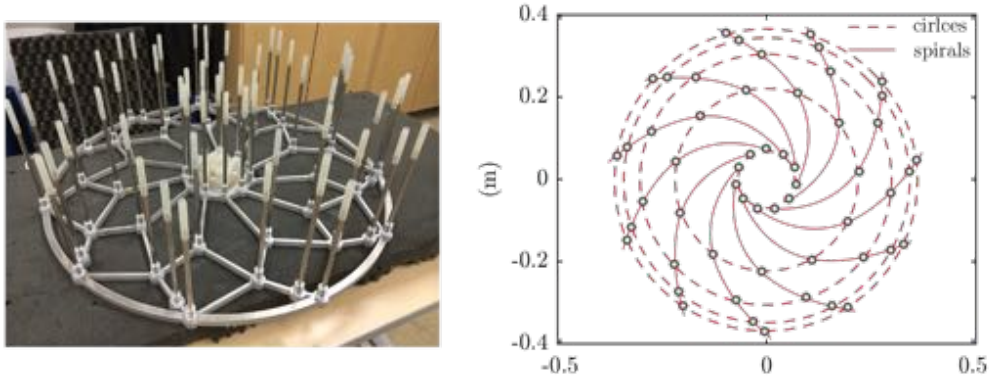

Fig. 7 Microphone array skeletal frame (left) and layout showing design criteria (right) [23].

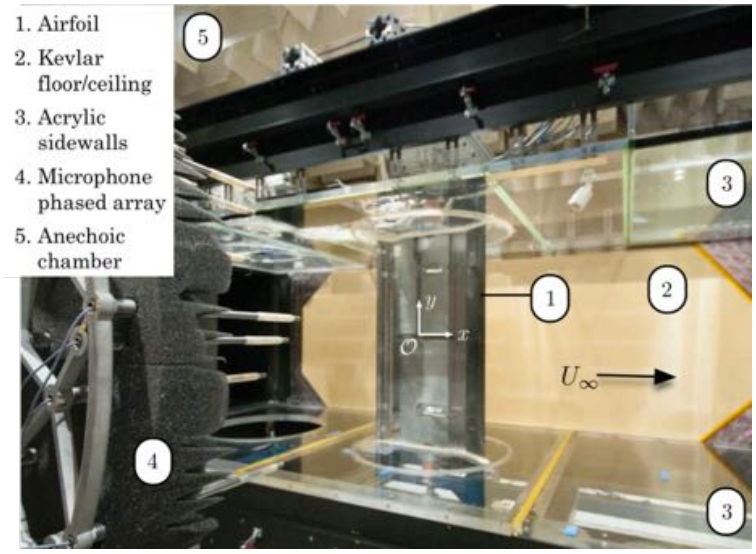

Fig. 8 Image of far-field acoustic measurement setup adapted from [23]. The Kevlar wall between the airfoil and the acoustic array is not shown in the picture. The center of the array is pointing at the middle of the rotation axis of the airfoil.

The array is located 1.18 m from the airfoil at zero angle of attack and centered on its axis of rotation ($x = 0.5c$ with respect to the stowed leading edge) as shown in Figure 8. The microphone array faces the pressure side of the airfoil to measure the radiated sound in a flyover configuration. During the measurements, the Pitot probe located upstream is traversed out of the test section to avoid corruption of the acoustic data. The data are sampled using multiple NI 4462 (24-bit) cards installed in the PXI 1045 chassis at 204.8 kHz for 60 seconds simultaneously. Prior to the measurements, the sensitivity of each microphone is calibrated using a Brüel and Kjær pistonphone (Type 4220) at 250 Hz [23]. An acoustic correction due to the transmission through the Kevlar wall is also applied [23].

DAS beamforming was also utilized to quantify the noise sources associated with the high level noise in the single microphone spectra. The source map visualization is superimposed on the wind tunnel schematic, whose background is illustrated in Figure 9. The flow direction is from left to right. The leading and trailing edges of the airfoil are projected on the $x - y$ plane as a function of the angle of attack. The top and bottom side walls are the bounds for the vertical domain, with the full length of the test section included. The source map domain for DAS is set to be $x \in$[-1 m,1 m] and $y \in$[-0.457 m,0.457 m] with a resolution of 0.005 m. Examples of the point spread function (PSF) along with the frequency-dependent 3-dB beamwidth are shown in Figure 10. The spatial resolution of noise sources is poor at low

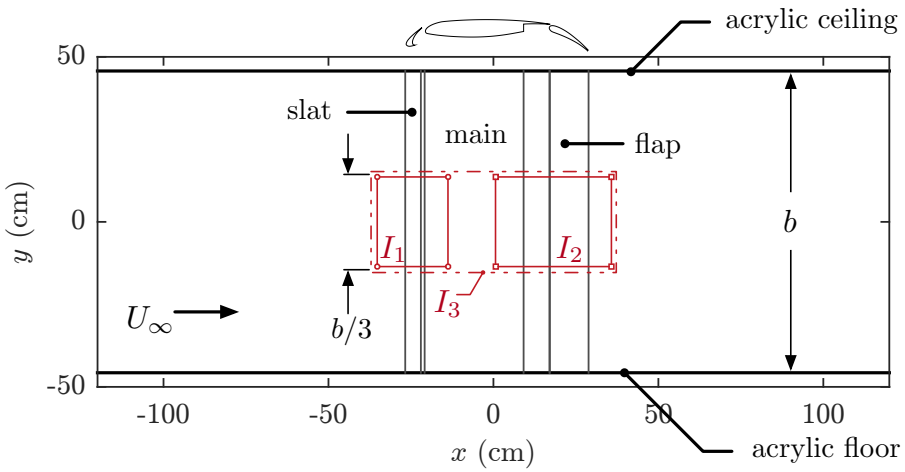

Fig. 9 Definition of regions used in integrated spectra [23].

frequency (i.e., below $1kHz$), with 3-dB beamwidth of greater than 0.6 m. As the frequency is increased, the resolution improves, but the number of sidelobes also increases due to spatial aliasing (Figure 10c to 10e) [23].

Spatial integration of acoustic fluctuations are performed on specific regions on the airfoil to eliminate contaminant noise as shown in Figure 9, where region I_1, I_2, and I_3 represent the center 1/3rd span of the slat, flap, and the whole airfoil, respectively. These locations are chosen to understand the relative contribution of the slat on the total acoustic signature of the airfoil as described in [23].

III. Results and discussion

In this section, each treatment will be assessed individually, including steady/unsteady surface pressure characteristics and the far-field acoustic behavior.

A. Slat extensions

The C_p distributions for different slat extensions are compared with the baseline case as shown in Figure 11. Due to similar behavior at other Reynolds numbers, only the results at $Re_c = 1.2e6$ are presented. To simplify the comparison, the pressure distributions are only compared using the pressure taps along the centerline of the airfoil. For the slat extensions, separation is delayed as the slat cusp is extended by the treatment. As a result, the trajectory and the reattachment of the shear layer are altered at off design conditions. As expected, the pressure distribution on the leading edge and suction side are barely affected. The shortest slat extension (Figure 11a to 11c) has negligible effect on the pressure distribution at $\alpha_k = 8°$ and even at $\alpha_k = 10°$. As the slat cusp extension increases, it has a larger effect on the pressure distribution due to the change in the shear layer trajectory. The change in the pressure distribution within the cove region is rather small, yet detectable, at the design angle of attack corresponding to $\alpha_k = 8°$. The magnitude of change becomes larger with increasing departure in the angle of attack, so that the effect of slat extension is most clearly observed at the largest angle of attack (15.5°) (Figure 11c, 11f, and 11i). In the C_p distribution along the centerline of the entire airfoil, shown in Figure 12, a decrease in C_p, corresponding to increased lift production, near the main element leading edge ($x/c \approx 0.05$) is observed. However, this small change barely affects the lift coefficient on the airfoil as shown in Figure 13.

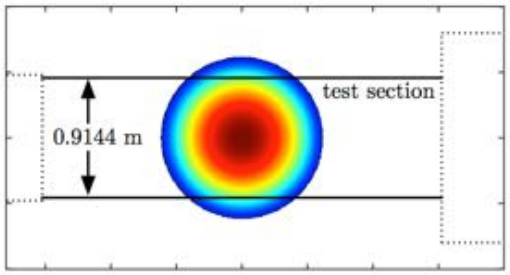

(a) 1 kHz

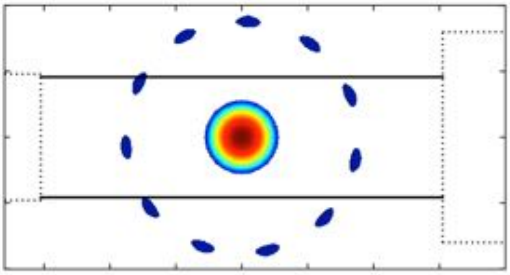

(b) 2 kHz

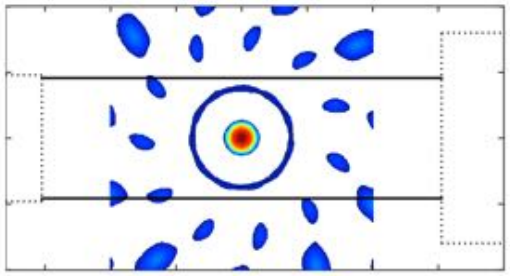

(c) 4 kHz

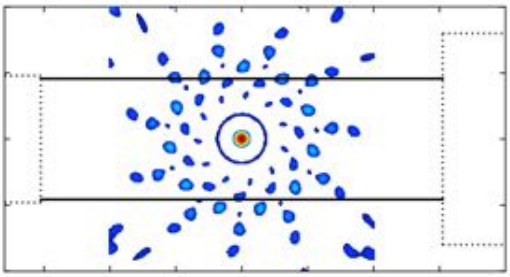

(d) 8 kHz

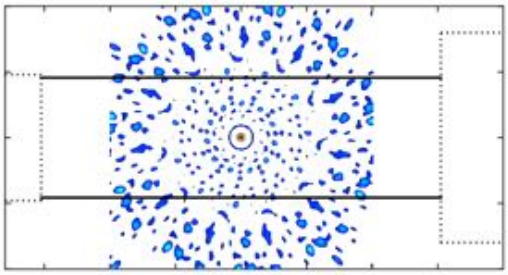

(e) 16 kHz

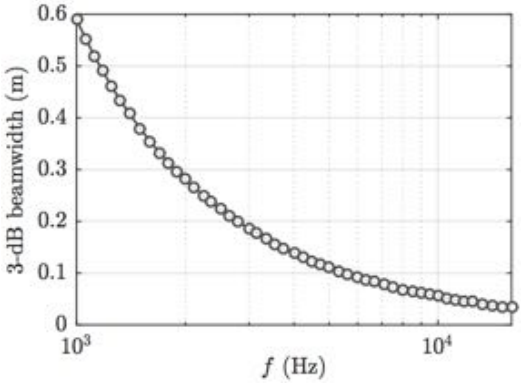

(f) 3-dB beamwidth resolution vs. f

Fig. 10 Point spread function (PSF) for 1, 2, 4, 8, and 16 kHz plotted with 15 dB dynamic range. The test section boundaries are provided for reference [23].

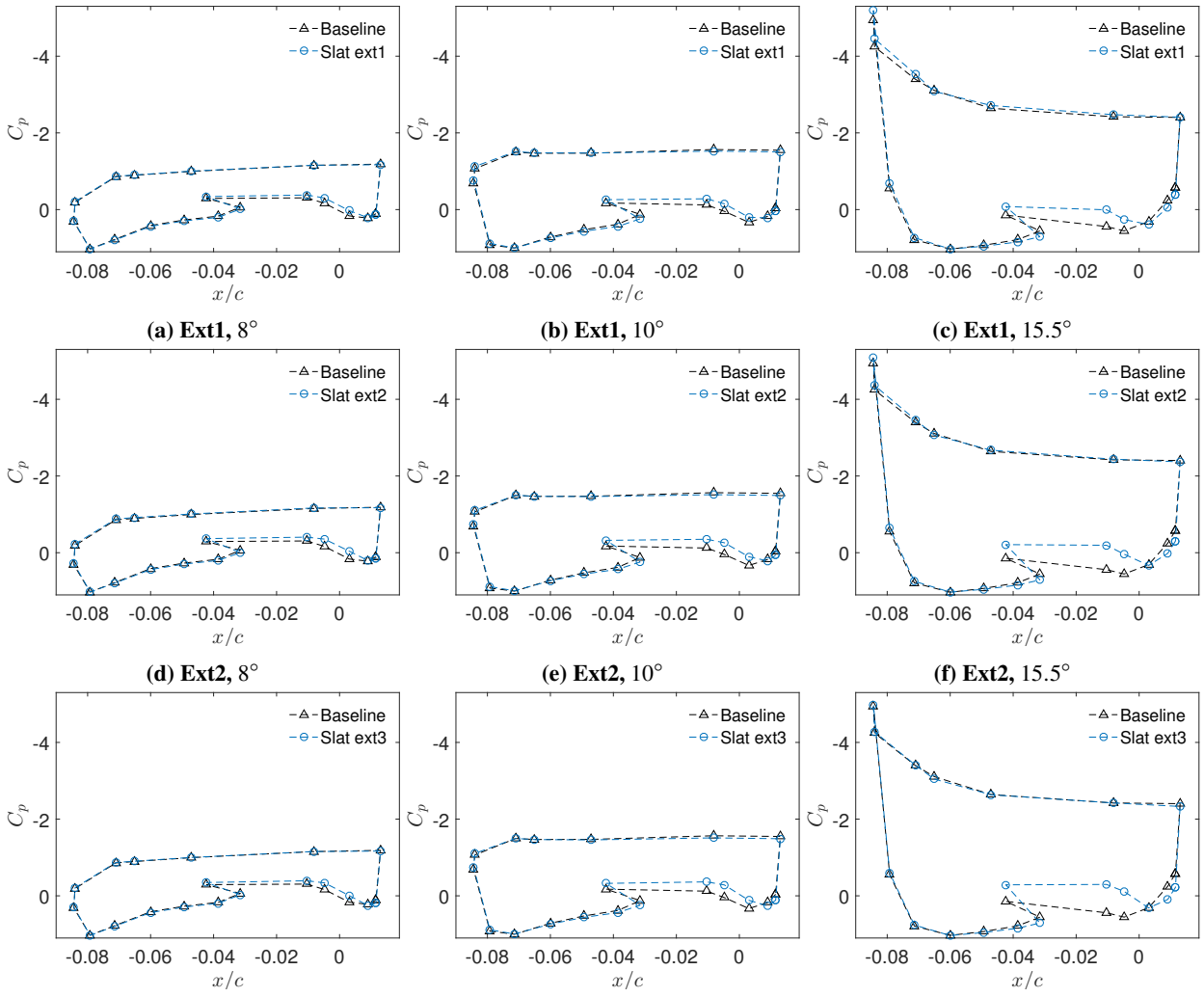

(a) Ext1, 8° **(b) Ext1,** 10° **(c) Ext1,** 15.5°

(d) Ext2, 8° **(e) Ext2,** 10° **(f) Ext2,** 15.5°

(g) Ext3, 8° **(h) Ext3,** 10° **(i) Ext3,** 15.5°

Fig. 11 C_p distribution on the slat with different extensions at $Re_c = 1.2e6$.

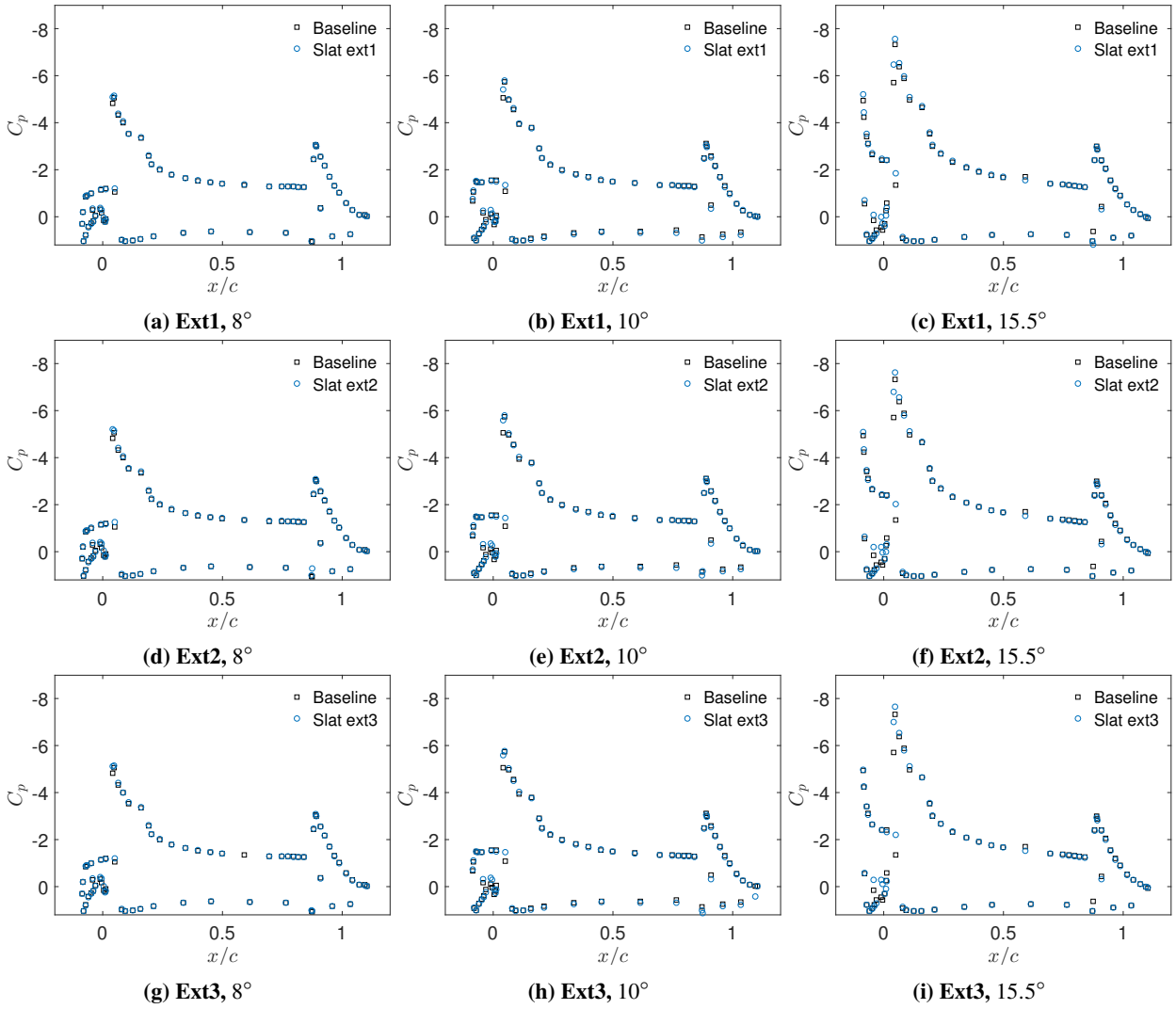

(a) Ext1, 8° **(b) Ext1,** 10° **(c) Ext1,** 15.5°

(d) Ext2, 8° **(e) Ext2,** 10° **(f) Ext2,** 15.5°

(g) Ext3, 8° **(h) Ext3,** 10° **(i) Ext3,** 15.5°

Fig. 12 C_p distribution along the centerline with different extensions at $Re_c = 1.2e6$.

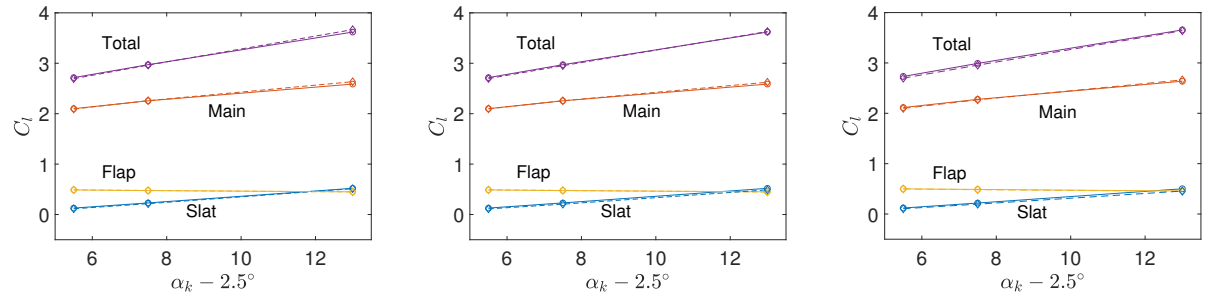

(a) Ext1 **(b) Ext2** **(c) Ext3**

Fig. 13 C_l calculated from centerline pressure taps with different extensions at $Re_c = 1.2e6$. Solid lines indicate the baseline case, and the dashed lines indicate the controlled case.

The surface pressure spectra, corresponding to the Kulite locations shown in Table 2, for the slat extension cases are compared with the baseline data and presented in Figures 14 to 16. The frequency is non-dimensionalized as $St_s = fs/U_\infty$. The spectral amplitudes are non-dimensionalized as $\hat{G}_{p,p} \cdot (U_\infty/s/q^2)$, where $\hat{G}_{p,p}$ is the estimate of power spectral density of the pressure fluctuations. All treatments have very similar effects on the pressure fluctuations, and the key features are highlighted as follows.

- Reductions are observed at the design condition of $\alpha_k = 8°$ at all sensor locations for all extensions. However, the pressure fluctuations are comparable at the off-design condition of $\alpha_k = 10°$ and even increased near the trailing edge of the slat at $\alpha_k = 15.5°$.
- The lowest frequency peak ($St_s \approx 0.15$) at all angles of attack is greatly suppressed, especially at the probe location P_2 that is just above the slat cusp. It is likely due to the stabilization of the shear layer flapping as the trajectory path is shortened.
- The resonances due to the shear layer instability are suppressed in $\alpha_k = 8°$ and $10°$ cases, and the peaks are shifted to higher St_s. The suppression is likely due to the shortening of the shear layer path such that the growth of disturbances is decreased. The higher St_s is due to the shortening of the shear layer path and the acoustic feedback path, resulting in higher frequencies of resonance.
- The longest slat extension (Ext3) yields the most effective suppression on the resonances associated with shear layer modes.
- The increase in the pressure fluctuations at $\alpha_k = 15.5°$ is likely due to the reattachment location of the shear layer having moved closer to the sensor locations.

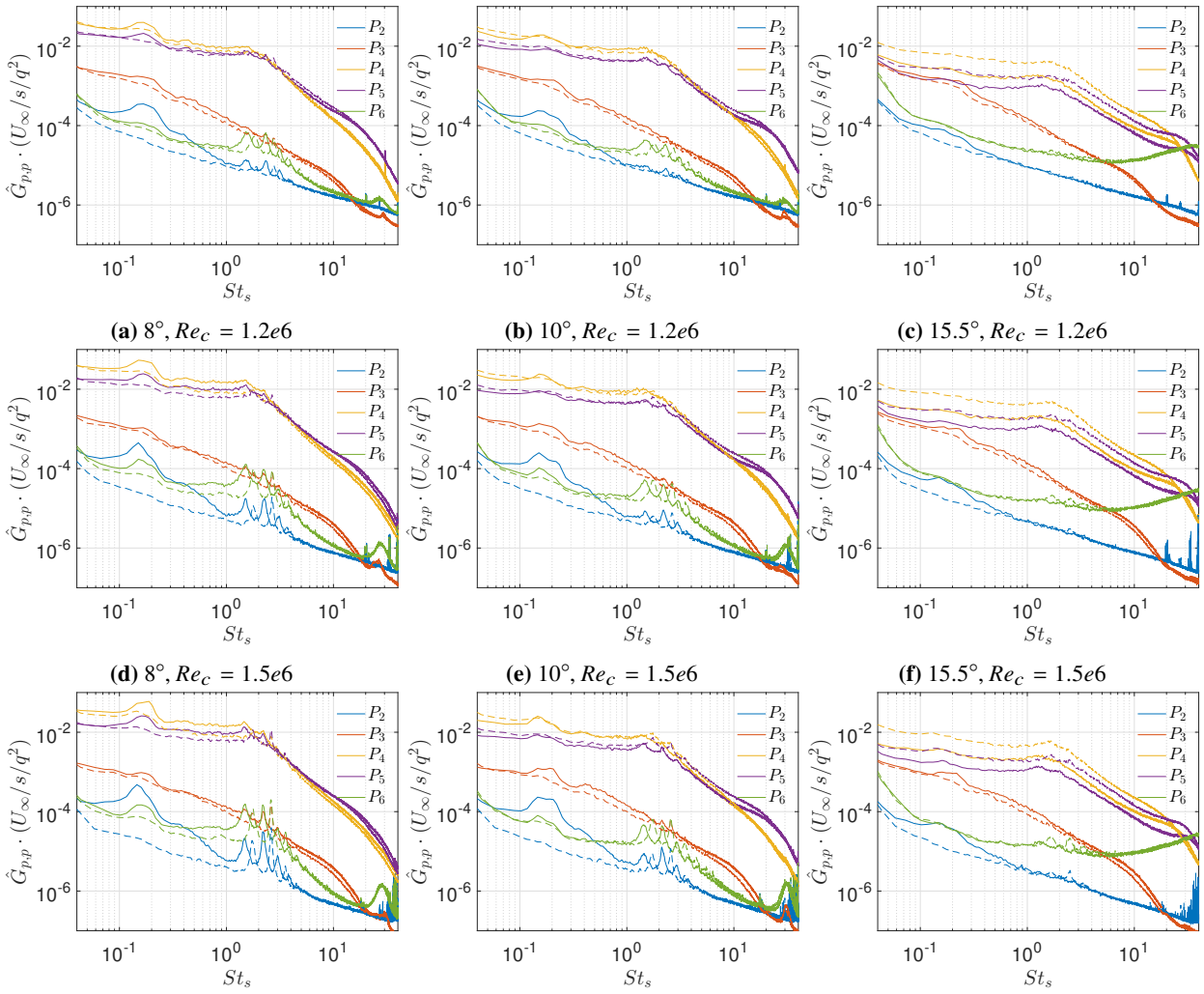

(a) 8°, Re_c = 1.2e6 **(b)** 10°, Re_c = 1.2e6 **(c)** 15.5°, Re_c = 1.2e6

(d) 8°, Re_c = 1.5e6 **(e)** 10°, Re_c = 1.5e6 **(f)** 15.5°, Re_c = 1.5e6

(g) 8°, Re_c = 1.71e6 **(h)** 10°, Re_c = 1.71e6 **(i)** 15.5°, Re_c = 1.71e6

Fig. 14 Spectra of surface fluctuating pressure for slat Ext1 at different Reynolds numbers. Solid and dashed lines represent the baseline and treatment cases, respectively.

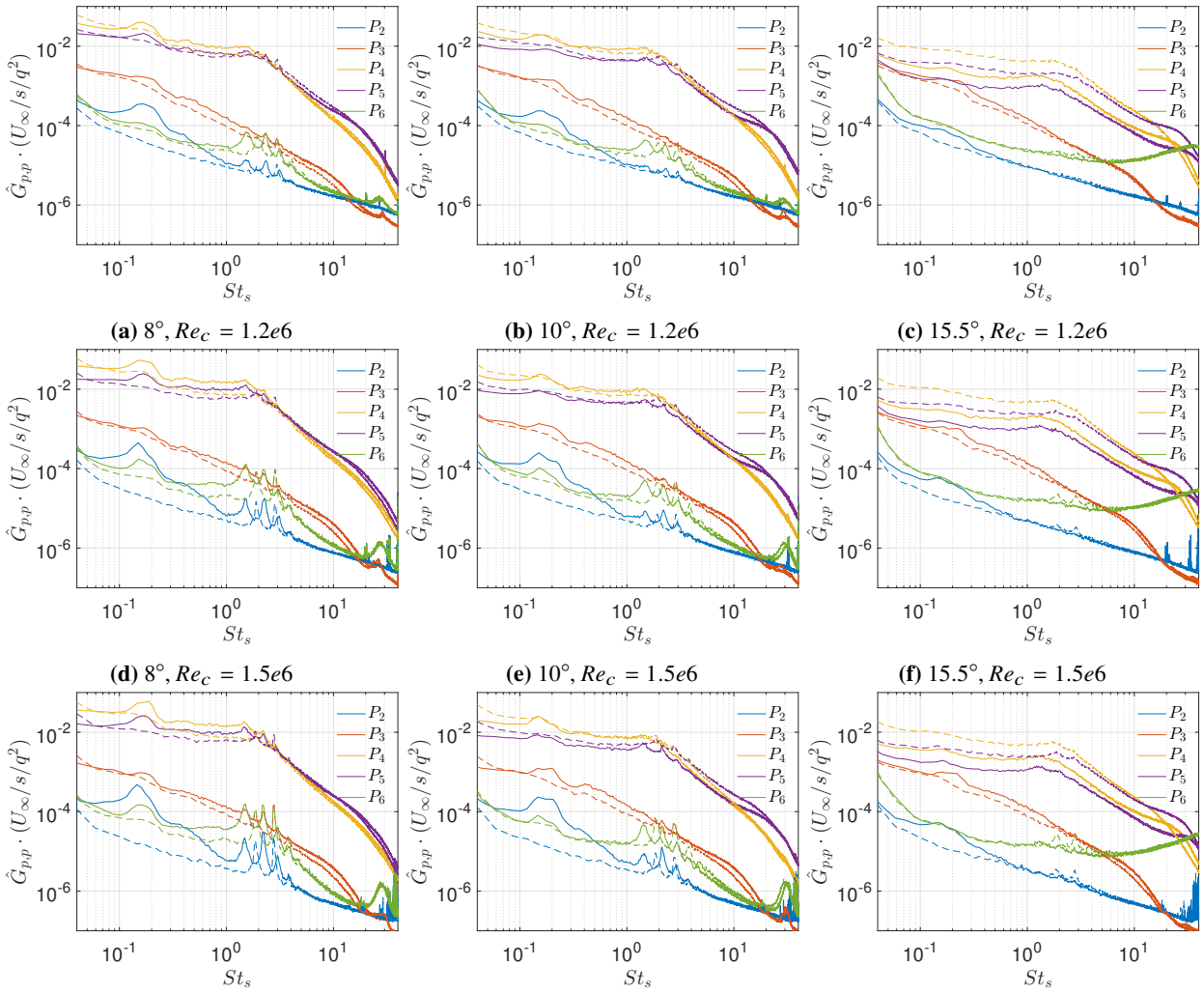

(a) 8°, Re_c = 1.2e6 **(b)** 10°, Re_c = 1.2e6 **(c)** 15.5°, Re_c = 1.2e6

(d) 8°, Re_c = 1.5e6 **(e)** 10°, Re_c = 1.5e6 **(f)** 15.5°, Re_c = 1.5e6

(g) 8°, Re_c = 1.71e6 **(h)** 10°, Re_c = 1.71e6 **(i)** 15.5°, Re_c = 1.71e6

Fig. 15 Spectra of surface fluctuating pressure for slat Ext2 at different Reynolds numbers. Solid and dashed lines represent the baseline and treatment cases, respectively.

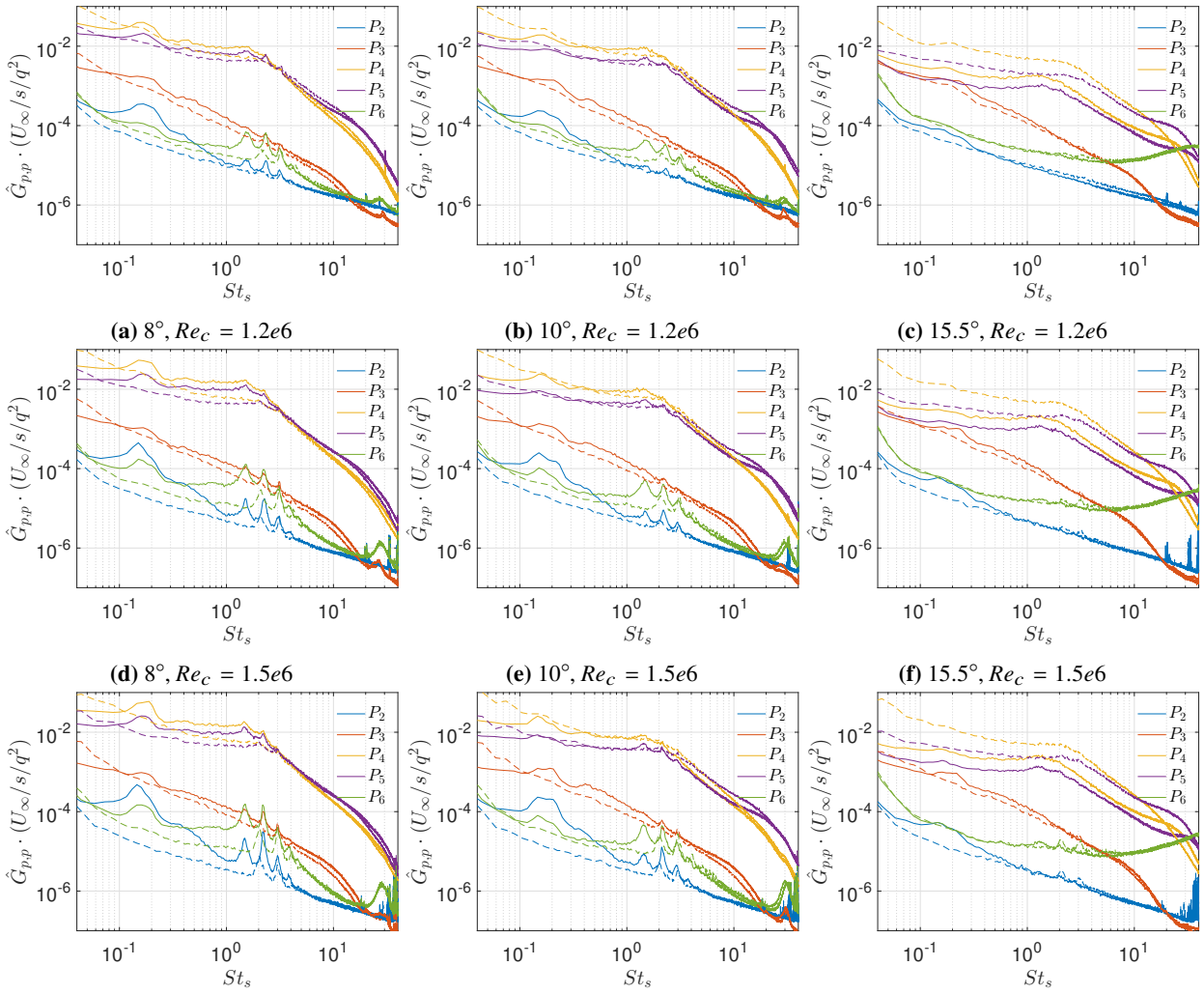

(a) 8°, Re_c = 1.2e6 **(b)** 10°, Re_c = 1.2e6 **(c)** 15.5°, Re_c = 1.2e6

(d) 8°, Re_c = 1.5e6 **(e)** 10°, Re_c = 1.5e6 **(f)** 15.5°, Re_c = 1.5e6

(g) 8°, Re_c = 1.71e6 **(h)** 10°, Re_c = 1.71e6 **(i)** 15.5°, Re_c = 1.71e6

Fig. 16 Spectra of surface fluctuating pressure for slat Ext3 at different Reynolds numbers. Solid and dashed lines represent the baseline and treatment cases, respectively.

It is instructive to examine the beamforming maps at the characteristic frequencies in the flow field, for example, the tones introduced by the shear layer instability in the baseline and the slat cusp extension cases. Therefore, the source maps for the first three tonal peaks observed in the previous surface pressure spectra are examined. Due to the large test matrix, only the results for all angles of attack at $Re_c = 1.2e6$ are provided in Figures 17 to 19. For the baseline cases, the high noise regions are distributed along the span of the slat at $\alpha_k = 8°$. With increasing α_k, the noise generated from the slat becomes less intense, making the boundary effects on the top and the bottom side walls more significant. The shortest slat extension (ext1) has the weakest effects on the source map. The longest slat extension (ext3) reduces the noise level due to the slat cove, and a higher percentage of the measured noise is now associated with interactions related to spanwise end effects.

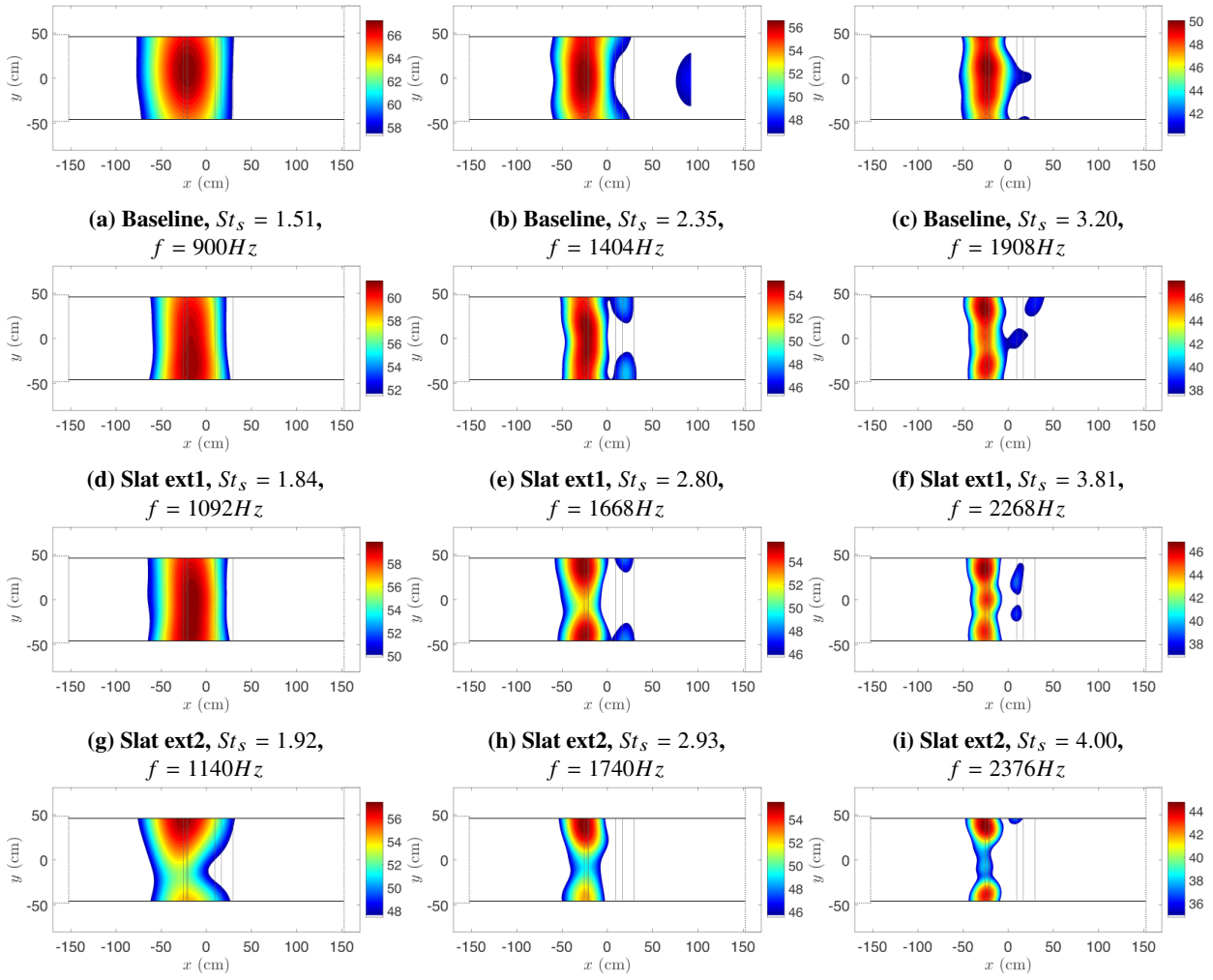

(a) Baseline, $St_s = 1.51$, $f = 900Hz$ **(b) Baseline,** $St_s = 2.35$, $f = 1404Hz$ **(c) Baseline,** $St_s = 3.20$, $f = 1908Hz$

(d) Slat ext1, $St_s = 1.84$, $f = 1092Hz$ **(e) Slat ext1,** $St_s = 2.80$, $f = 1668Hz$ **(f) Slat ext1,** $St_s = 3.81$, $f = 2268Hz$

(g) Slat ext2, $St_s = 1.92$, $f = 1140Hz$ **(h) Slat ext2,** $St_s = 2.93$, $f = 1740Hz$ **(i) Slat ext2,** $St_s = 4.00$, $f = 2376Hz$

(j) Slat ext3, $St_s = 2.19$, $f = 1296Hz$ **(k) Slat ext3,** $St_s = 3.26$, $f = 1932Hz$ **(l) Slat ext3,** $St_s = 4.42$, $f = 2616Hz$

Fig. 17 Source maps for $\alpha_k = 8°$ at $Re_c = 1.2 \times 10^6$ for narrowband DAS with 10 dB dynamic range relative to peak level. The center frequencies correspond to the first three shear layer modes introduced by the slat cusp.

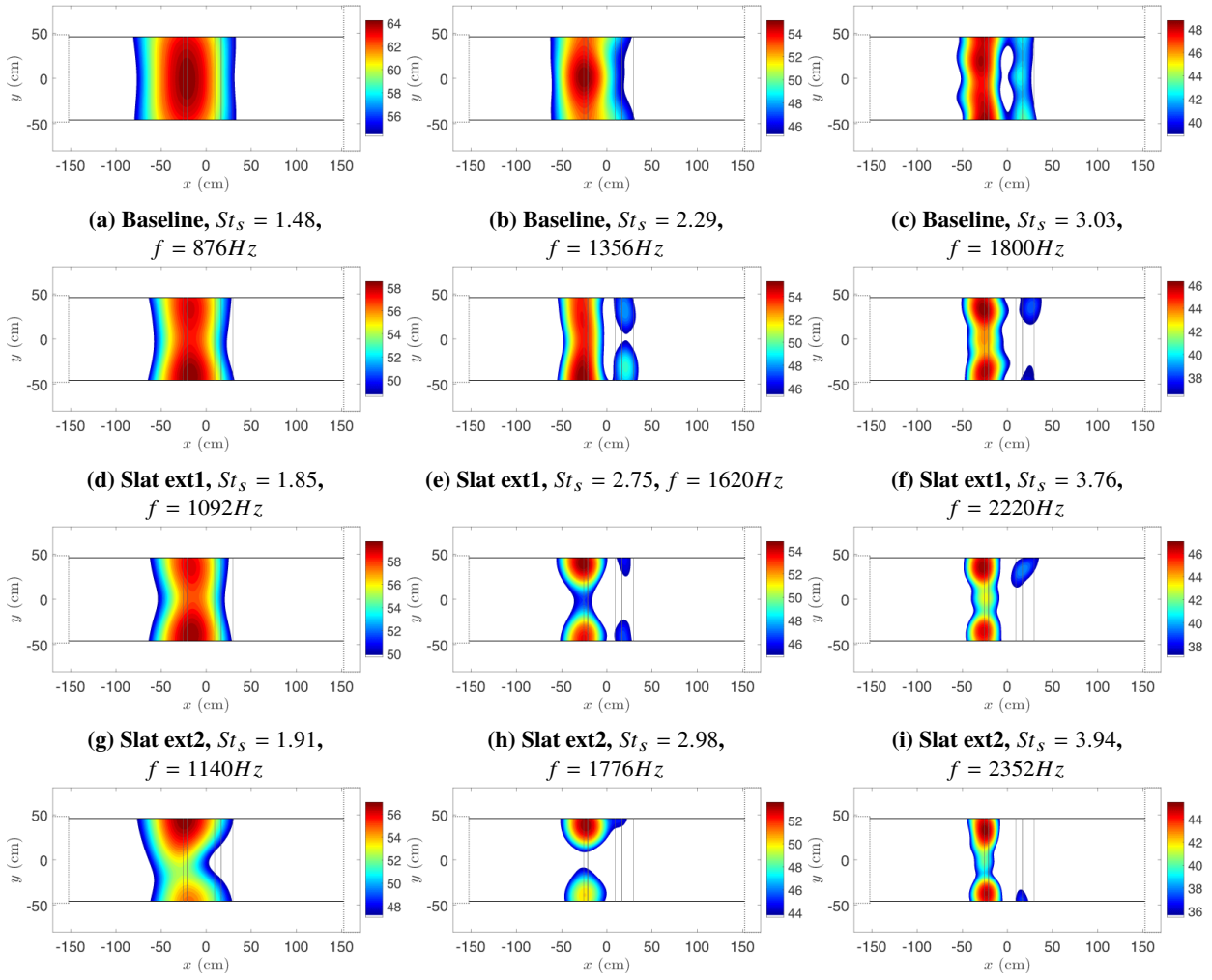

(a) Baseline, $St_s = 1.48$, $f = 876Hz$ **(b) Baseline,** $St_s = 2.29$, $f = 1356Hz$ **(c) Baseline,** $St_s = 3.03$, $f = 1800Hz$

(d) Slat ext1, $St_s = 1.85$, $f = 1092Hz$ **(e) Slat ext1,** $St_s = 2.75$, $f = 1620Hz$ **(f) Slat ext1,** $St_s = 3.76$, $f = 2220Hz$

(g) Slat ext2, $St_s = 1.91$, $f = 1140Hz$ **(h) Slat ext2,** $St_s = 2.98$, $f = 1776Hz$ **(i) Slat ext2,** $St_s = 3.94$, $f = 2352Hz$

(j) Slat ext3, $St_s = 2.17$, $f = 1296Hz$ **(k) Slat ext3,** $St_s = 3.35$, $f = 2004Hz$ **(l) Slat ext3,** $St_s = 4.31$, $f = 2580Hz$

Fig. 18 Source maps for $\alpha_k = 10°$ at $Re_c = 1.2 \times 10^6$ for narrowband DAS with 10 dB dynamic range relative to peak level. The center frequencies correspond to the first three shear layer modes introduced by the slat cusp.

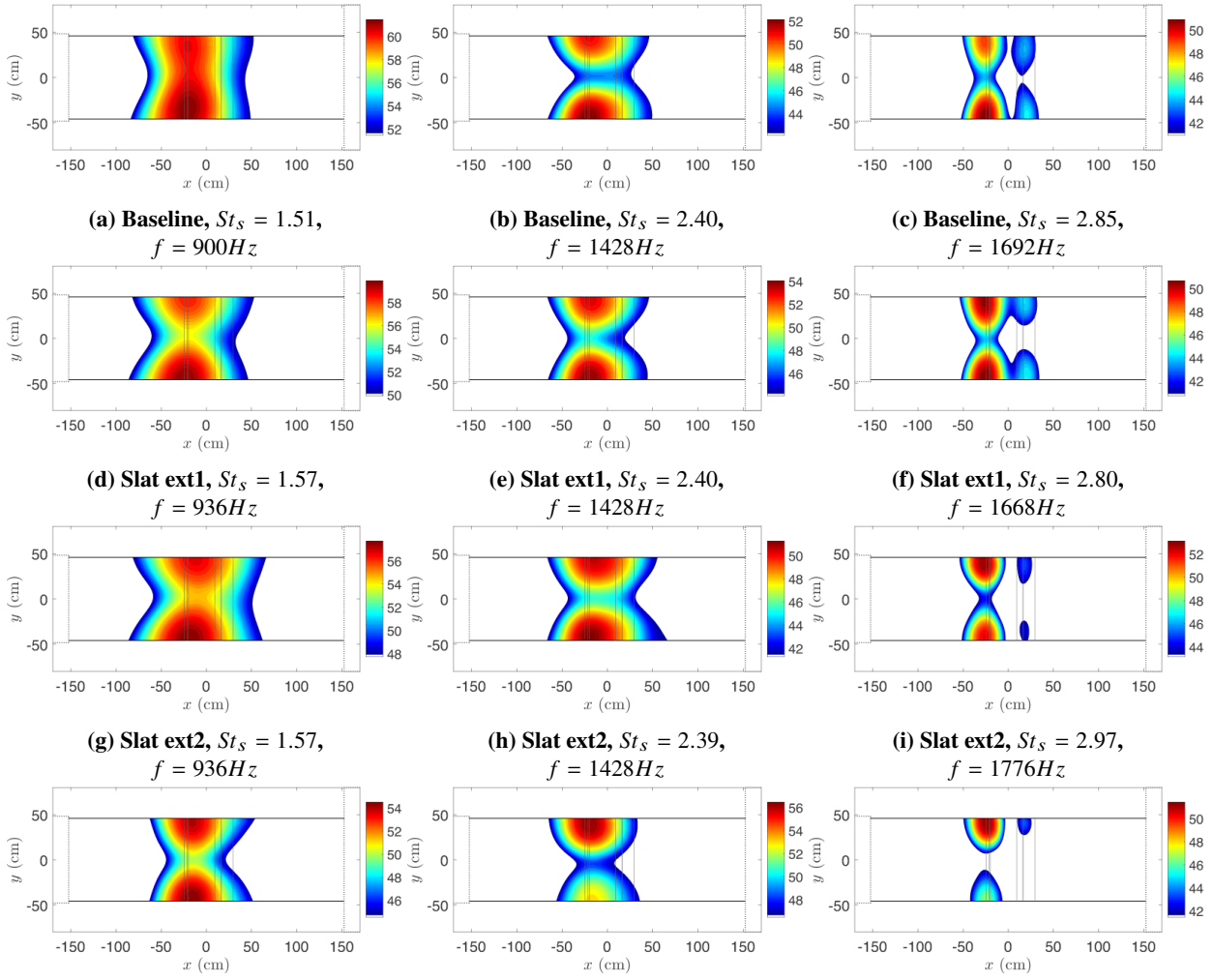

(a) Baseline, $St_s = 1.51$, $f = 900Hz$ **(b) Baseline, $St_s = 2.40$, $f = 1428Hz$** **(c) Baseline, $St_s = 2.85$, $f = 1692Hz$**

(d) Slat ext1, $St_s = 1.57$, $f = 936Hz$ **(e) Slat ext1, $St_s = 2.40$, $f = 1428Hz$** **(f) Slat ext1, $St_s = 2.80$, $f = 1668Hz$**

(g) Slat ext2, $St_s = 1.57$, $f = 936Hz$ **(h) Slat ext2, $St_s = 2.39$, $f = 1428Hz$** **(i) Slat ext2, $St_s = 2.97$, $f = 1776Hz$**

(j) Slat ext3, $St_s = 1.90$, $f = 1140Hz$ **(k) Slat ext3, $St_s = 2.38$, $f = 1428Hz$** **(l) Slat ext3, $St_s = 3.40$, $f = 2040Hz$**

Fig. 19 Source maps for $\alpha_k = 15.5°$ at $Re_c = 1.2 \times 10^6$ for narrowband DAS with 10 dB dynamic range relative to peak level. The center frequencies correspond to the first three shear layer modes introduced by the slat cusp.

The integrated DAS beamforming over region I_1, as defined in Figure 9, between the baseline and controlled cases are shown in Figure 20. The sound pressure levels in the results are scaled to a 1 m span at 1 m observer distance. The three slat extensions are grouped into the same figure for comparison as shown in Figure 20. Similar to the near field pressure spectra obtained from the Kulite sensors, the SPL of shear layer modes are slightly reduced at 8° and 10°, and the frequencies are increased due to the shortened shear layer path. The treatments have no significant effect on the broadband noise for $St_s > 8$. In general, the longest slat extension (Ext3) provides the largest suppression at each Reynolds number and angle of attack. The change in the overall sound pressure level (OASPL) compared with the baseline case are listed in Table 3 for $Re_c = 1.71e6$.

B. Gap filler

The pressure distribution on the slat and the entire airfoil with the gap filler installed are shown in Figures 21 and 22, respectively. It is clear that the gap filler significantly alters the aerodynamic performance of the airfoil. Specifically, it decreases the suction peak over the main element and the flap, especially at the highest angle of attack (Figure 22c). Recall that the decision to implement the gap filler without modifying the leading edge of the main wing may have resulted in a small gap between the gap filler and the main wing and that gap could have widened in the course of the test

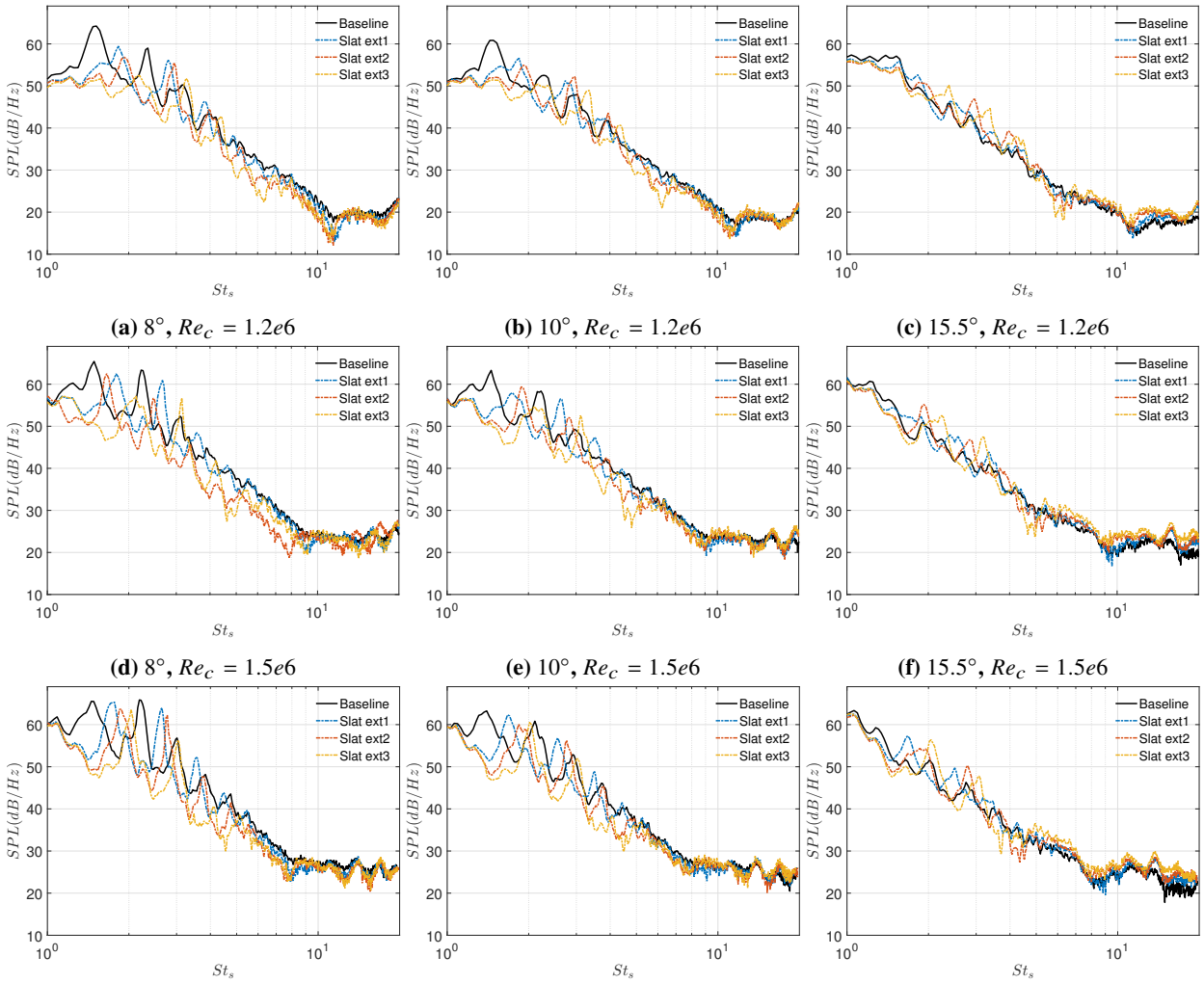

(a) 8°, $Re_c = 1.2e6$ **(b)** 10°, $Re_c = 1.2e6$ **(c)** 15.5°, $Re_c = 1.2e6$

(d) 8°, $Re_c = 1.5e6$ **(e)** 10°, $Re_c = 1.5e6$ **(f)** 15.5°, $Re_c = 1.5e6$

(g) 8°, $Re_c = 1.71e6$ **(h)** 10°, $Re_c = 1.71e6$ **(i)** 15.5°, $Re_c = 1.71e6$

Fig. 20 Comparison of integrated DAS beamforming between baseline and slat extension cases from region I_1 in the Kevlar test section. The sound pressure levels are scaled to a 1 m span at 1 m observer distance.

Table 3 Δ OASPL (dB) change with different slat extensions at $Re_c = 1.71e6$.

α_k	8°	10°	15°
Slat ext1	-0.9	-0.8	0
Slat ext2	-2.5	-1.6	-0.4
Slat ext3	-3.2	-1.6	0.6

campaign. In that case, the gap would have resulted in a jet of high-speed flow that acted to separate the boundary layer on the suction side of the main wing. A similar behavior has been observed for a different but related condition when the slat approaches the main wing during retraction, as reported by Scholten et al. [26]. The results in this section should be interpreted in the light of this limitation on the gap filler implementation in the present case. The pressure distribution is barely affected on the pressure side of the main element and the flap. The net effect is that the lift coefficient for the main wing is reduced by 1.17 at the 15.5° off-design condition after the gap filler was installed as shown in Figure 23. As the main element is the primary lift contributor, it is likely that the total lift coefficient will also decrease with this particular gap filler design, as a result of possible boundary layer separation due to the high-speed flow through the slit between the gap filler and the main wing. However, we also note that the gap filler concept of Turner et al [12, 27] is intended to deploy dynamically during the landing phase, and therefore, the aerodynamic degradation at off-design conditions should not have major consequence as long as the gap filler can be deployed and retracted in a reliable manner. It is difficult to discern from the measurements whether or not the gap filler design led to a pocket of separated flow behind the filler contour. However, even if it did, one expects that the directivity of the noise sources associated with flow unsteadiness in that region will be primarily focused in direction that point above the airfoil, rather than in the observer direction.

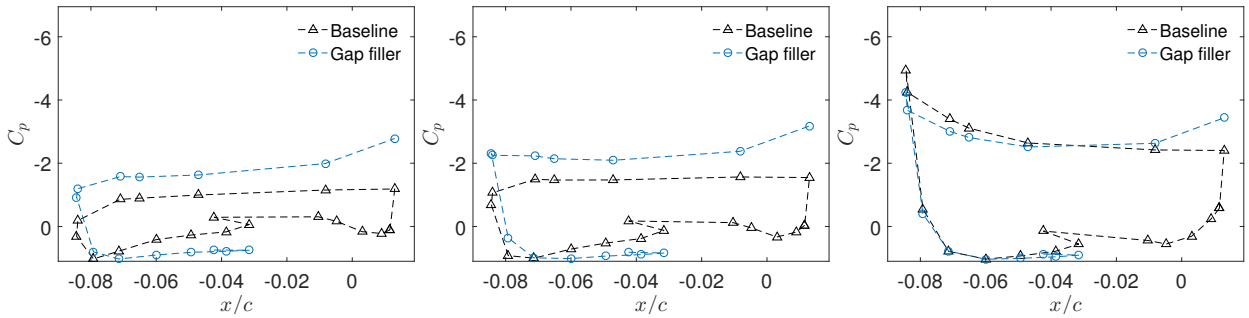

(a) 8° **(b)** 10° **(c)** 15.5°

Fig. 21 C_p distribution on the slat with the gap filler installed at $Re_c = 1.2e6$. Covered pressure ports are not plotted.

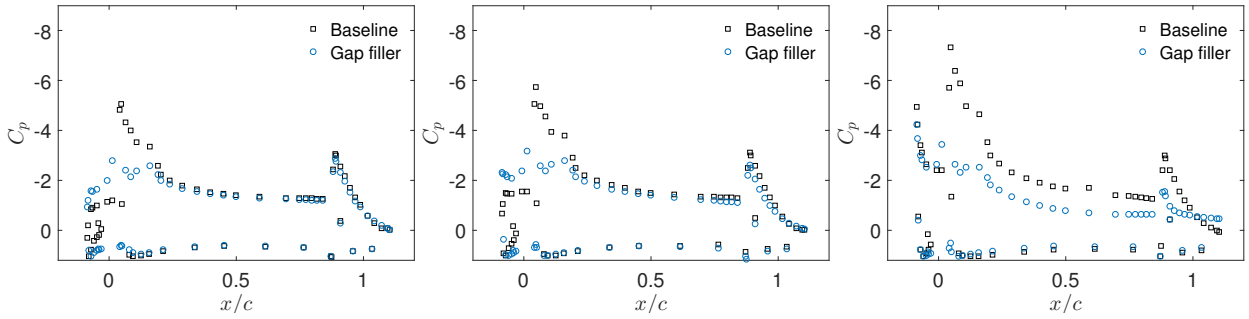

(a) 8° **(b)** 10° **(c)** 15.5°

Fig. 22 C_p distribution along the centerline with the gap filler installed at $Re_c = 1.2e6$.

Unsteady surface pressure spectra for the gap filler case are shown in Figure 24. The gap filler eliminates the pumping or breathing effect through the gap due to its blockage. In addition, the gap filler also stops the flow from separating at the slat trailing edge at small angles of attack. Therefore, the pressure fluctuations associated with the shear layer instability are suppressed at $\alpha_k = 8°$ and 10°. The pressure fluctuations are generally reduced at all sensor locations. However, it is unclear if the fluctuations on the slat are reduced due to the alteration of the cavity feedback mechanism or because of a lack of sensors on the gap filler. It should be noted that the pressure spectra obtained from P_6 look noisy at $Re_c = 1.5e6$ and $1.71e6$. First, it was suspected that there were some issues with the sensor. However, the tests are repeated at different Reynolds numbers, and these phenomena only happen at high Reynolds numbers with high reproducibility. One possibility is that the thin extension may vibrate during the tests at high Reynolds numbers,

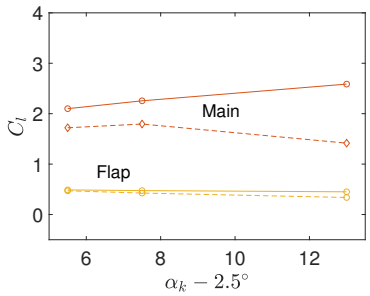

Fig. 23 C_l calculated from centerline pressure taps with the gap filler installed at $Re_c = 1.2e6$. Lift on the slat cannot be calculated because several pressure taps are covered with the gap filler installed. Solid lines indicate the baseline case, and the dashed lines indicate the controlled case.

and thus it introduced some disturbances in the flow field. The effects on the near field pressure fluctuations are similar to the far-field signature, which are provided in the following discussions. Essentially, the gap filler suppresses the shear layer modes within $St_s = 1$ to 3. However, it introduces a strong broadband hump in the high frequency portion of the measured spectra, potentially because the tiny slit between the main element and the gap filler trailing edge begins to whistle, especially when Re_c is increased, as the high-pressure flow begins to seep through the gap. The mechanism for this needs to be investigated further using flow field diagnostic methods.

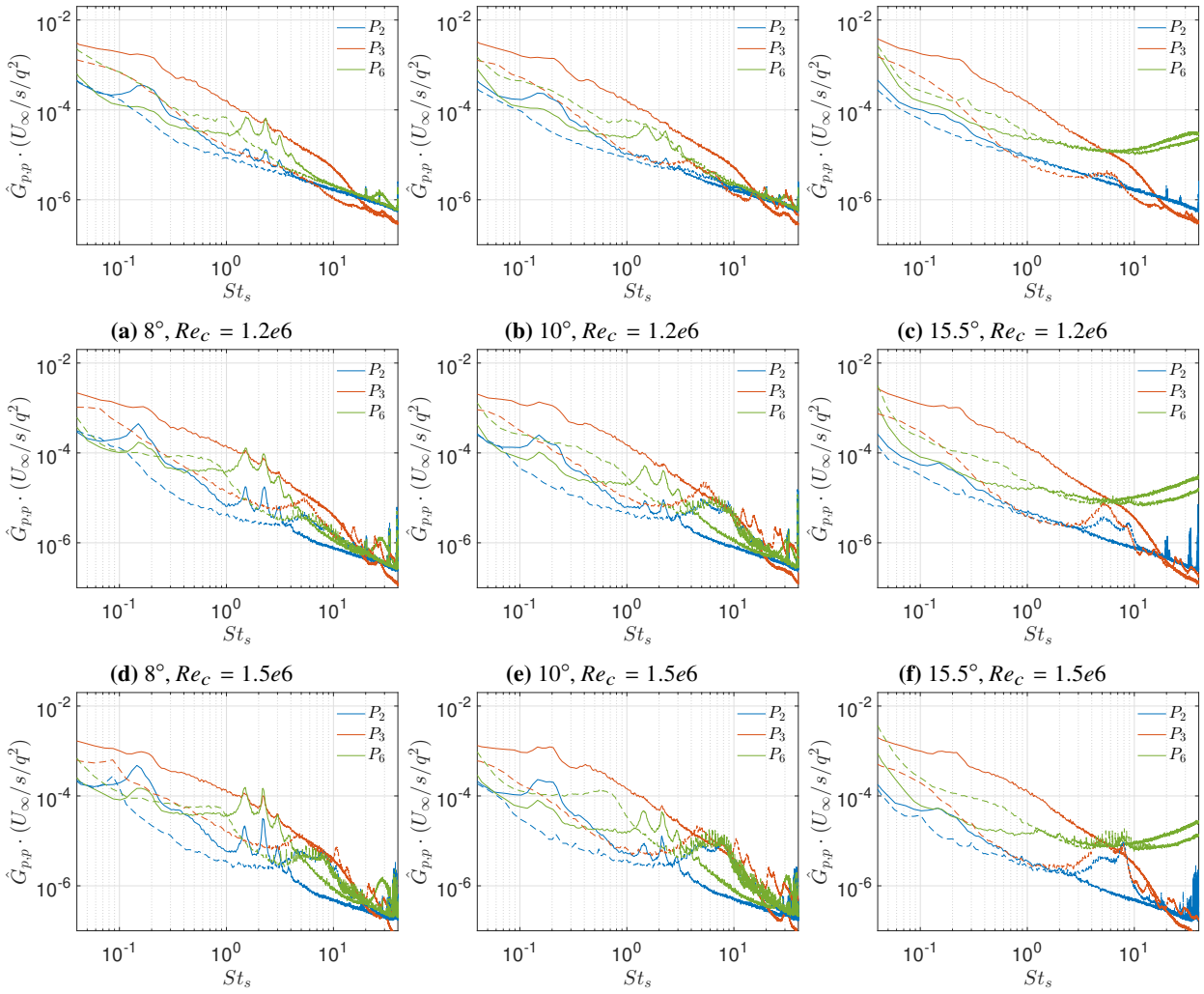

(a) 8°, Re_c = 1.2e6 **(b)** 10°, Re_c = 1.2e6 **(c)** 15.5°, Re_c = 1.2e6

(d) 8°, Re_c = 1.5e6 **(e)** 10°, Re_c = 1.5e6 **(f)** 15.5°, Re_c = 1.5e6

(g) 8°, Re_c = 1.71e6 **(h)** 10°, Re_c = 1.71e6 **(i)** 15.5°, Re_c = 1.71e6

Fig. 24 Spectra of surface fluctuating pressure for gap filler cases. Solid and dashed lines represent the baseline and treatment cases, respectively.

No clear characteristic frequency is observed in the surface pressure spectra for the gap filler case as all the tonal peaks are suppressed. Some broadband humps are found at the frequencies of the original tonal peaks. These peaks along with the broadband hump are visualized via DAS beamforming as shown in Figure 25. The source maps for $St_s \approx 2.4$ show some high noise regions located at the center of the slat. At $St_s \approx 7$, the noise sources are more distributed along the slat.

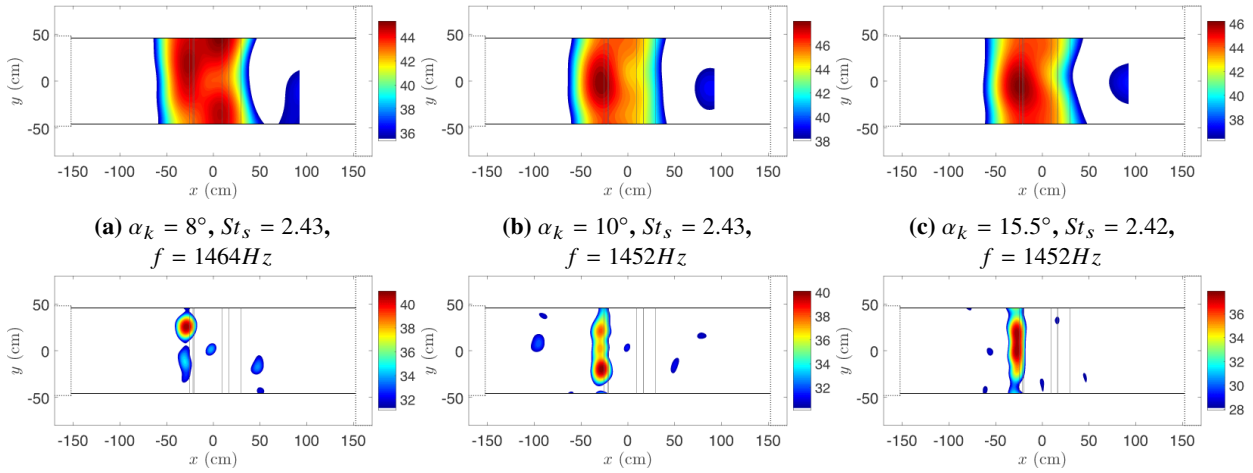

(a) $\alpha_k = 8°$, $St_s = 2.43$, $f = 1464Hz$ **(b)** $\alpha_k = 10°$, $St_s = 2.43$, $f = 1452Hz$ **(c)** $\alpha_k = 15.5°$, $St_s = 2.42$, $f = 1452Hz$

(d) $\alpha_k = 8°$, $St_s = 6.79$, $f = 4092Hz$ **(e)** $\alpha_k = 10°$, $St_s = 6.78$, $f = 4044Hz$ **(f)** $\alpha_k = 15.5°$, $St_s = 6.94$, $f = 4164Hz$

Fig. 25 Source maps for gap filler at $Re_c = 1.2 \times 10^6$ for narrowband DAS with 10 dB dynamic range relative to peak level.

The integrated DAS beamforming are compared with the baseline case as shown in Figure 26. Although the gap filler suppress the peaks for $St_s < 3$, a hump is introduced between $St_s = 3$ and 10 as a penalty of the control. Beyond $St_s > 10$, there are several peaks, similar to the spectra obtained from Kulite sensor at P_3 location located inside the slat cove. Without further investigations of the flow field, the origin of these peaks remains unknown at this stage. Even though the gap filler introduces extra broadband noise at higher frequencies, the OASPL is reduced by 2.4dB at the primary AoA of interest, namely $\alpha_k = 8°$. As mentioned before, improvements in gap filler design and a successful seal for the slit between the gap filler and the main element should allow one to minimize the aerodynamic penalty of this device. Thus, if the cause behind the increased noise levels at higher frequencies can be identified and tackled, then the gap filler concept would become more appealing.

Table 4 Δ OASPL (dB) change with gap filler at $Re_c = 1.71e6$.

α_k	8°	10°	15°
Δ OASPL (dB)	-2.4	0.5	-0.9

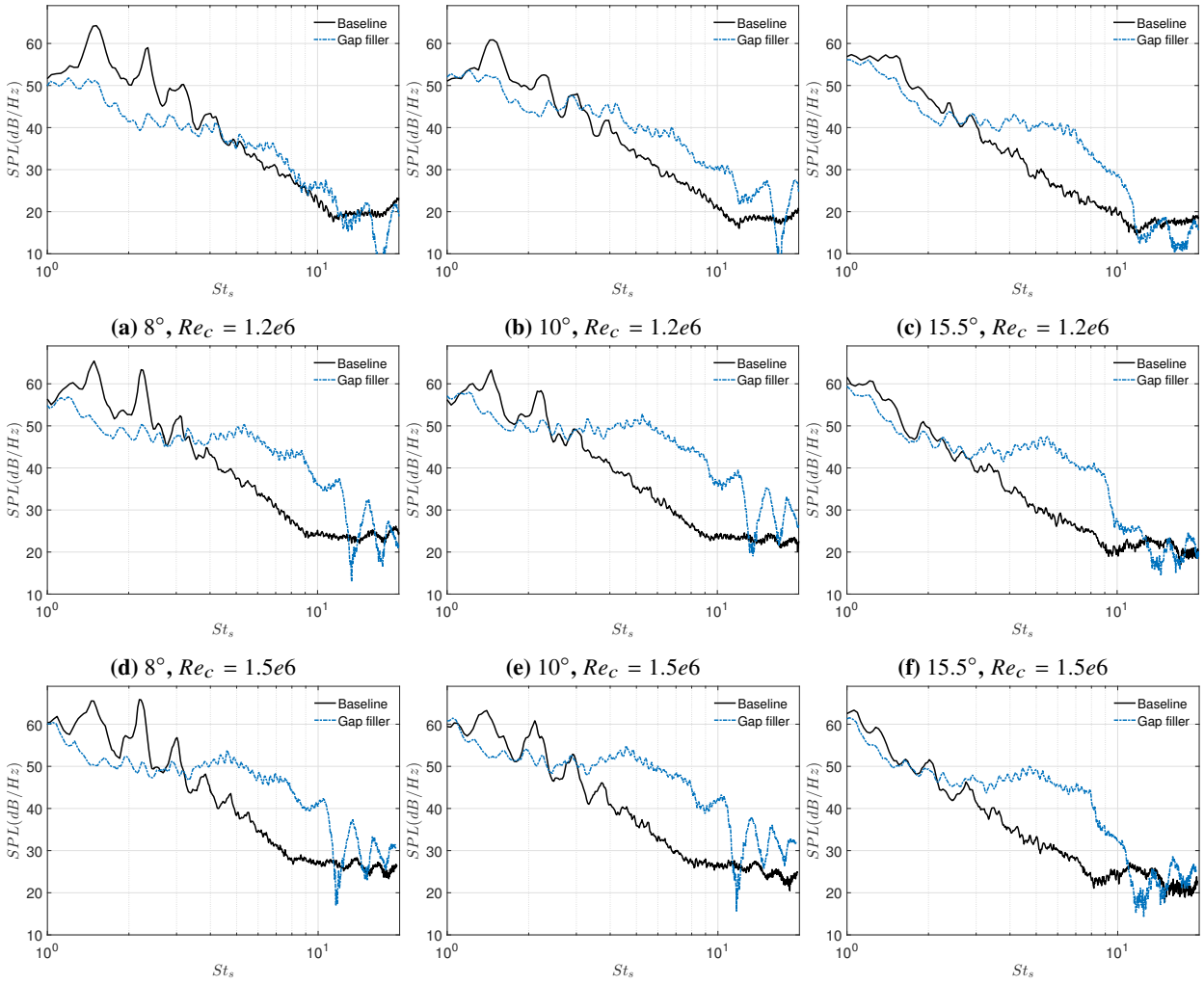

(a) 8°, $Re_c = 1.2e6$ **(b)** 10°, $Re_c = 1.2e6$ **(c)** 15.5°, $Re_c = 1.2e6$

(d) 8°, $Re_c = 1.5e6$ **(e)** 10°, $Re_c = 1.5e6$ **(f)** 15.5°, $Re_c = 1.5e6$

(g) 8°, $Re_c = 1.71e6$ **(h)** 10°, $Re_c = 1.71e6$ **(i)** 15.5°, $Re_c = 1.71e6$

Fig. 26 Comparison of integrated DAS beamforming between baseline and gap filler cases from region I_1 in the Kevlar test section. The sound pressure levels are scaled to a 1 m span at 1 m observer distance.

C. Cove filler

The pressure distribution of the cove filler cases are shown in Figures 27 and 28. Generally, the cove filler had a rather small influence on the pressure distribution on the slat, even at off design angles of attack. The change on the pressure side cannot be fully assessed due to a lack of pressure taps on the cove filler surface. The cove filler clearly alters the separation on the pressure side of the slat. Thus, it also alters the breathing/pumping effects through the gap. As a result, the pressure near the main element leading edge is reduced within a very small area on the suction side with a negligible change on the pressure side. As shown in Figure 29, the cove filler has very weak effect on the lift coefficient on the main element and the flap. As the main element is the primary lift contributor, it is likely that the cove filler will weakly affect the total lift coefficient.

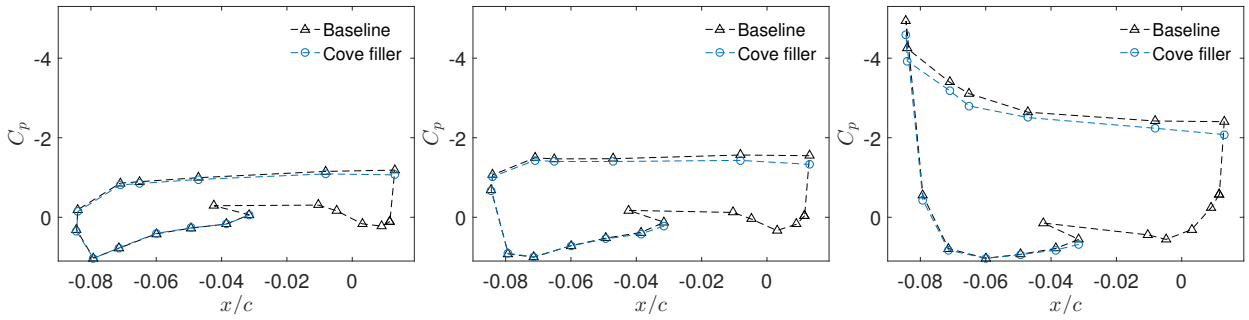

(a) 8° **(b)** 10° **(c)** 15.5°

Fig. 27 C_p **distribution on the slat with the cove filler installed at** $Re_c = 1.2e6$**.**

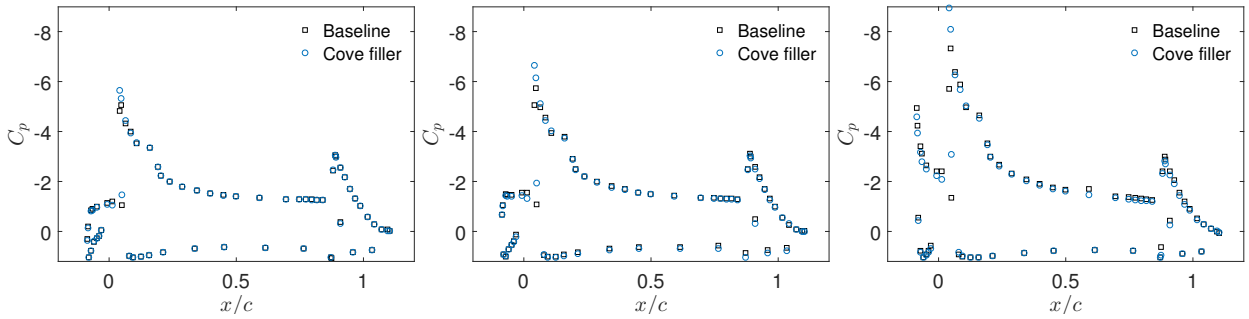

(a) 8° **(b)** 10° **(c)** 15.5°

Fig. 28 C_p **distribution along the centerline with the cove filler installed at** $Re_c = 1.2e6$**. Covered pressure ports are not plotted.**

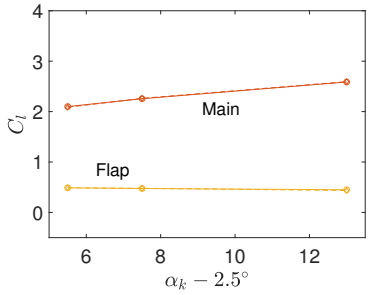

Fig. 29 C_l **calculated from centerline pressure taps with the cove filler installed at** $Re_c = 1.2e6$**. Solid lines indicate the baseline case, and the dashed lines indicate the controlled case.**

Unsteady surface pressure spectra for the cove filler case are shown in Figure 30. Only the Kulite sensors, P_2 and P_3 are left exposed to the flow in the presence of the cove filler. These two sensors are located near the slat cusp and the slat trailing edge, respectively. Unfortunately, P_2 sensor was apparently damaged during the experiments; thus the spectra for this location are missing for suspect cases. During the experiments, the sensors underneath the cove filler also measured some pressure fluctuations, indicating that the cove filler was not perfectly sealed to the cove wall. However, a sealant could not be used as it added a finite thickness between the cove filler and slat, resulting in a slight but noticeable change of the geometry at the slat trailing edge. As expected, the tonal peaks associated with the shear layer instability do not exist as the region of flow separation is drastically reduced in size. The suppression effects are significant at the low angles of attack, while only slight suppression is observed at P_2 for $St_s = 0.2$ at the highest angle of attack. Without measuring the unsteady fluctuating pressure on the cove filler surface, only very limited information is available about the dominant noise sources contributing to the near field acoustic signature at P_2 and P_6.

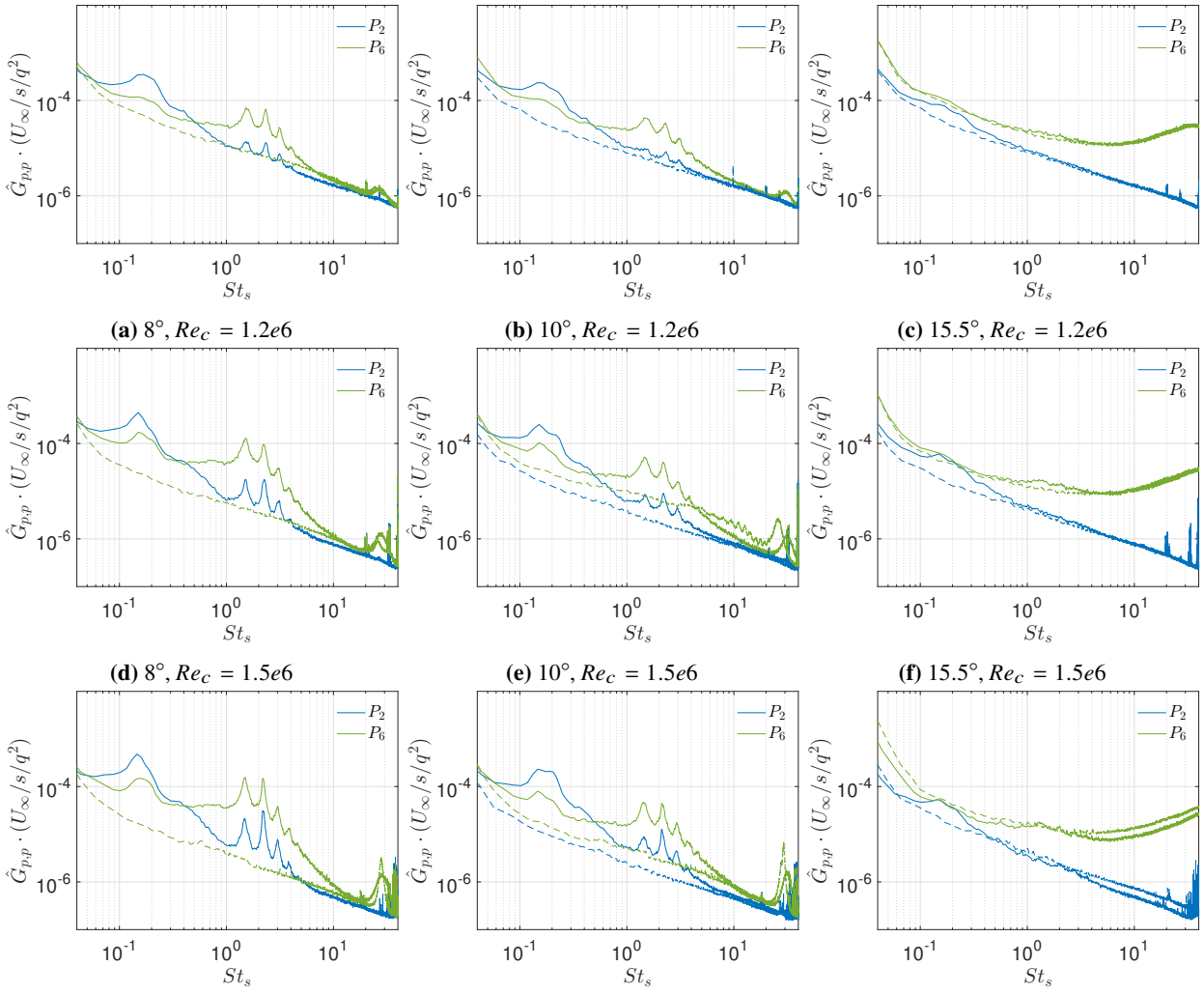

(a) 8°, $Re_c = 1.2e6$ **(b)** 10°, $Re_c = 1.2e6$ **(c)** 15.5°, $Re_c = 1.2e6$

(d) 8°, $Re_c = 1.5e6$ **(e)** 10°, $Re_c = 1.5e6$ **(f)** 15.5°, $Re_c = 1.5e6$

(g) 8°, $Re_c = 1.71e6$ **(h)** 10°, $Re_c = 1.71e6$ **(i)** 15.5°, $Re_c = 1.71e6$

Fig. 30 Spectra of surface fluctuating pressure for cove filler cases. Solid and dashed lines represent the baseline and treatment cases, respectively.

The cove filler case has an unexpected story for the acoustic signature. Initially, there were multiple mysterious peaks/spikes observed in the spectra of the far-field pressure fluctuations with the treatment as shown in Figure 31. Based on the literature and flow physics, the presence of these peaks was not expected for this configuration. The DAS beamforming maps show these peaks originated from locations near the center of the slat, which did not make physical

sense. First, it was suspected that there was a small but finite gap between the cove filler and slat due to machining tolerances. However, the use of silicone and masking tape sealant between these two metal pieces did not remove these peaks. Close inspection revealed a small step between the slat cusp and the cove filler; so this step was subsequently covered by masking tape to achieve a smooth transition. It was found that this procedure significantly suppressed the peaks at high Reynolds numbers, although some sharp peaks still existed at $Re_c = 1.2e6$. It was also found that these peaks are sensitive to the tape texture, and rough tape exhibits better suppression than smooth tape. Since the roughness had some effect on the acoustic signature, boundary layer zig-zag trip (BL trip) was attached to the slat cusp located just upstream of the step as shown in Figure 4b. The comparison of different treatments on the slat and cove filler are provided in Figure 31. It is clear that the spectra of the tape and BL trip cases are very close at high Reynolds numbers. However, the BL trip eliminates the peaks that show up in the masking tape case at $Re_c = 1.2e6$.

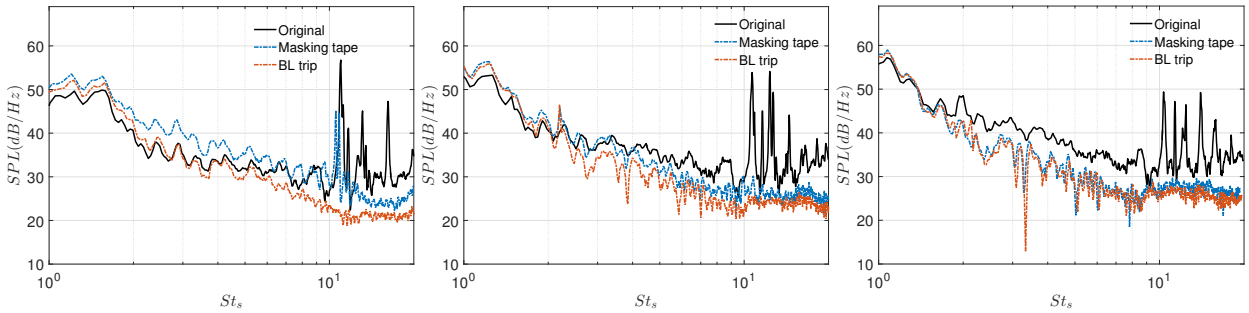

(a) $Re_c = 1.2e6$ **(b)** $Re_c = 1.5e6$ **(c)** $Re_c = 1.71e6$

Fig. 31 Comparison of integrated DAS beamforming between different treatments applied in the cove filler cases at $\alpha_k = 8°$ from region I_1 in the Kevlar test section. The sound pressure levels are scaled to a 1 m span at 1 m observer distance.

The effects of the cove filler on the integrated spectra are compared with the baseline cases as shown in Figure 32. The tones associated with the shear layer modes no longer exist as the flow does not separate from the slat cusp. In addition, it barely introduces any negative side effects at $\alpha_k = 8°$ and $10°$ for all Reynolds numbers. However, it increases the broadband noise level at the off-design conditions of $\alpha_k = 15.5°$. The OASPL differences are listed in table 5, showing promising noise reduction effects. Overall, the cove filler appears to provide the best noise suppression along all three treatments. However, similar to the gap filler, the present measurements do not provide any insights into the dominant source(s) of residual noise levels measured in the presence of the cove filler.

Table 5 Δ OASPL (dB) change with cove filler and BL trip at $Re_c = 1.71e6$.

α_k	8°	10°	15°
Δ OASPL (dB)	-3.9	-2.1	-1.1

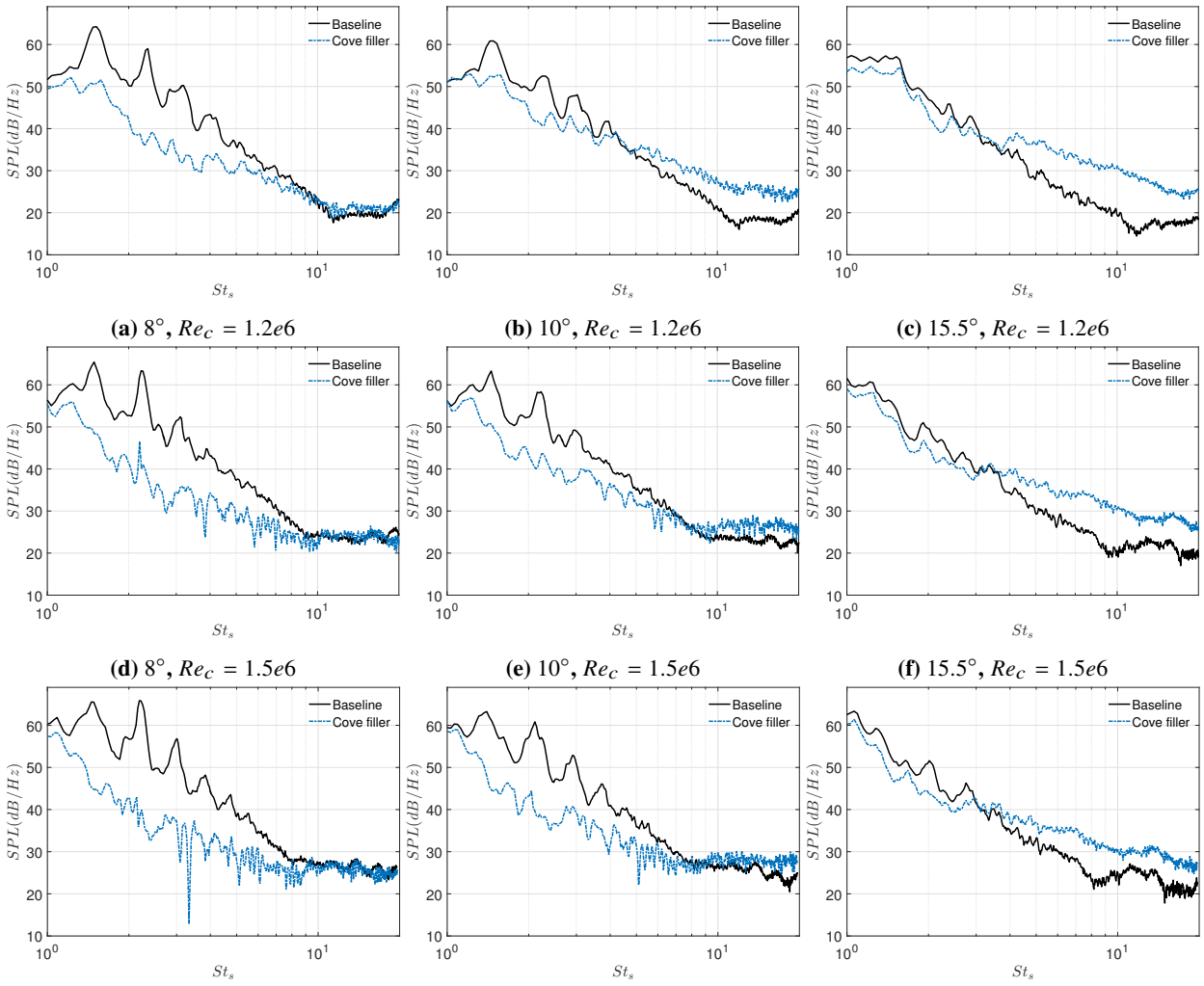

(a) 8°, $Re_c = 1.2e6$ **(b)** 10°, $Re_c = 1.2e6$ **(c)** 15.5°, $Re_c = 1.2e6$

(d) 8°, $Re_c = 1.5e6$ **(e)** 10°, $Re_c = 1.5e6$ **(f)** 15.5°, $Re_c = 1.5e6$

(g) 8°, $Re_c = 1.71e6$ **(h)** 10°, $Re_c = 1.71e6$ **(i)** 15.5°, $Re_c = 1.71e6$

Fig. 32 Comparison of integrated DAS beamforming between baseline and cove filler cases from region I_1 in the Kevlar test section. BL trip is attached to the slat surface. The sound pressure levels are scaled to a 1 m span at 1 m observer distance.

IV. Conclusions

Three different types of passive devices, slat extension, gap filler, and cove filler, are tested to evaluate their performance with regard to the aerodynamics and the slat noise from the two-dimensional, 30P30N high-lift configuration used in the BANC series of workshops. The experiments are conducted at three angles of attack and Reynolds numbers, with the measurements including both steady and unsteady surface pressures and far-field acoustics.

All three lengths of slat extensions have similar effects on the flow field, specifically by shortening the shear layer path originating at the slat cusp such that the overall growth of the shear layer instability is suppressed. The extensions exhibit weak effects on the mean C_p distribution at the design condition of $\alpha_k = 8^\circ$ and modestly off design condition of $\alpha_k = 10^\circ$, while they have greater effects on the pressure distribution near the slat cove and the main element leading edge at the significantly off design condition of $\alpha_k = 15.5^\circ$. The extensions suppress the tonal peaks as well as shifting them to higher frequencies for all test cases. However, the pressure fluctuations increase near the slat trailing edge at $\alpha_k = 15.5^\circ$, which is likely due to the alteration of the shear layer trajectory. From the DAS beamforming and integrated spectra, the longest extension has better control effects on the noise level.

The gap filler attempts to eliminate the interaction between the unsteadiness in slat cove flow with the slat trailing edge and the gap region by blocking the gap between the slat and the main element. However, for the present gap filler design (which was not as streamlined as desired), the resulting changes in the unsteady flow field via a modification of the cavity feedback mechanism are also accompanied by negative effects on the mean C_p distribution. Additionally, the desire to leave the leading edge of the main wing of the model unmodified forced a gap filler implementation approach that left a small gap at the joint with the main wing. Attempts to close or seal the gap during experiments proved unsuccessful, which likely had an adverse impact on lift production near the leading edge of the main wing. Specifically, the suction peak near the main element leading edge is significantly reduced at $\alpha_k = 8^\circ$ and 10°, with the loss in suction peak becoming worse at the highest angle of attack, $\alpha_k = 15^\circ$. The tonal noise in the unsteady surface pressure spectra is eliminated. However, the gap filler introduces a broadband hump at higher frequencies at $Re_c = 1.5e6$ and $1.71e6$, which could be an artifact of the above mentioned gap, i.e., an adverse side effect of the suboptimal implementation of the gap filler, rather than an intrinsic feature of the concept. Similar effects of the gap filler are also observed in the far-field acoustic measurements for all tested cases. Therefore, the present gap filler design and model integration approach are not deemed to be an effective option for noise reduction. Future work should examine the influence of both improved gap filler design and of firmly attaching the gap filler to the main element during the measurements.

At the design condition corresponding to $\alpha_k = 8^\circ$, the mean Cp distribution with the cove filler is virtually unchanged from the baseline case with no cove filler. However, at the off design conditions corresponding to higher AOA, the cove filler increases the suction peak to a greater extent near the main element leading edge. Unfortunately, the changes in mean loading over the cove filler surface could not be assessed as there were no pressure taps on the treatment. Significant reduction in both narrowband peaks and the broadband spectrum are observed at the two Kulite sensors located at the slat leading edge and slat trailing edge, respectively, for both $\alpha_k = 8^\circ$ and $\alpha_k = 10^\circ$. The effects at the highest AOA is weak in that it reduces the broadband peak at $St_s = 0.2$. In the integrated spectra, the tonal peaks are totally eliminated by the cove filler. At the highest AOA ($\alpha_k = 15^\circ$), the cove filler design for $\alpha_k = 8^\circ$ leads to a slight increase in the broadband noise levels at higher frequencies. Yet, the broadband OASPL is reduced even at this highly off-design condition. Overall, the cove filler is the most effective passive device among the treatment designs that were tested during the present campaign.

Acknowledgments

The work reported here is performed under the NASA Contract NNL14AE67P. The authors would like to thank Mr. Christopher Cagle for his help with the hardware design of the slat brackets and all three noise reduction treatments, the NASA Langley Machine shop for fabricating the instrumented slat model as well as the treatments evaluated during the current work, and Dan Neuhart and Luther Jenkins for their generous advice with model assembly. Thanks are also due to the FSU machinists Bobby Avant and Adam Piotrowski for tunnel modifications

References

[1] Dobrzynski, W., "Almost 40 years of airframe noise research: What did we achieve?" *Journal of Aircraft*, Vol. 47, 2010, pp. 353–367.

[2] Khorrami, M. R., Berkman, M. E., and Choudhari, M., "Unsteady Flow Computations of a Slat with a Blunt Trailing Edge," *AIAA Journal*, Vol. 38, No. 11, 2000, pp. 2050–2058.

[3] Singer, B. A., Lockard, D. P., and Brentner, K. S., "Computational Aeroacoustic Analysis of Slat Trailing-Edge Flow," *AIAA Journal*, Vol. 38, No. 9, 2000, pp. 1558–1564.

[4] Terracol, M., Manoha, E., and Lemoine, B., "Investigation of the Unsteady Flow and Noise Generation in a Slat Cove," *AIAA Journal*, Vol. 54, No. 2, 2016, pp. 469–489.

[5] Pascioni, K. A., and Cattafesta, L. N., "Unsteady characteristics of a slat-cove flow field," *Phys. Rev. Fluids*, Vol. 3, 2018. doi:10.1103/PhysRevFluids.3.034607.

[6] Rossiter, J. E., "Wind-tunnel Experiments on the Flow over Rectangular Cavities at Subsonic and Transonic speeds," Tech. rep., Aeronautical Research Council Reports and Memoranda, 1964. No. 3438.

[7] Choudhari, M. M., and Khorrami, M. R., "Effect of Three-Dimensional Shear-Layer Structures on Slat Cove Unsteadiness," *AIAA Journal*, Vol. 45, No. 9, 2007, pp. 2174–2186.

[8] Knacke, T. J., and Thiele, F., "Numerical Analysis of Slat Noise Generation," *19th AIAA/CEAS Aeroacoustics Conference*, American Institute of Aeronautics and Astronautics, Reston, Virginia, 2013. AIAA paper 2013-2162.

[9] Choudhari, M., Lockard, D., Macaraeg, M., Singer, B., Streett, C., Neubert, G., Stoker, R., Underbrink, J., Berkman, M., Khorrami, M., and Sadowski, S., "Aeroacoustic experiments in the langley low-turbulence pressure tunnel," Tech. rep., NASA, 2002. TM 2002-211432.

[10] Streett, C. L., Casper, J. H., Lockard, D. P., Khorrami, M. R., Stoker, R. W., Elkoby, R., Wenneman, W. F., and Underbrink, J. R., "Aerodynamic noise reduction for high-lift devices on a swept wing model," 2006. AIAA Paper 2006-212.

[11] Imamura, T., Ura, H., Yokokawa, Y., Enomoto, S., Yamamoto, K., and Hirai, T., "Designing of slat cove filler as a noise reduction device for leading-edge slat," 2007. AIAA Paper 2007-3473.

[12] Turner, T. L., Khorrami, M. R., Lockard, D. P., McKenney, M. J., Atherley, R. D., and Kidd, R. T., "Multi-element airfoil system," U.S. Patent 8763958, July 2014.

[13] Bridges, J., and Brown, C. A., "Parametric Testing of Chevrons on Single Flow Hot Jets," 2004. AIAA Paper 2004-2824.

[14] Kopiev, V., Zaitsev, M., Belyaev, I., and Mironov, M., "Noise reduction potential through slat hook serrations," 2011. AIAA Paper 2011-2909.

[15] Smith, M., Chow, L., and Molin, N., "Attenuation of slat trailing edge noise using slat gap acoustic liners," 2006. AIAA Paper 2006-2666.

[16] Chappell, S., Cai, Z., Zhang, X., and Angland, D., "Slat Noise Feedback Control with a Dielectric Barrier Discharge Plasma Actuator," *6th AIAA Flow Control Conference*, American Institute of Aeronautics and Astronautics, Reston, Virigina, 2012. AIAA paper 2012-2806.

[17] Spaid, F. W., "High reynolds number, multielement airfoil flowfield measurements," *Journal of Aircraft*, Vol. 37, No. 3, 2000, pp. 499–507.

[18] Pascioni, K., Reger, R., Edstrand, A., and Cattafesta, L., "Characterization of an Aeroacoustic Wind Tunnel Facility," Vol. 249, 2014, pp. 3966–3975. 43rd International Congress on Noise Control Engineering.

[19] Choudhari, M. M., and Lockard, D. P., "Assessment of Slat Noise Predictions for 30P30N High-Lift Configuration from BANC-III Workshop," *21st AIAA/CEAS Aeroacoustics Conference*, American Institute of Aeronautics and Astronautics, Reston, Virginia, 2015. doi:doi:10.2514/6.2015-2844, aIAA Paper 2015-2844.

[20] Pascioni, K. A., and Cattafesta, L. N., "Aeroacoustic Measurements of Leading-Edge Slat Noise," *22nd AIAA/CEAS Aeroacoustics Conference*, American Institute of Aeronautics and Astronautics, Lyon, France, 2016.

[21] Khorrami, M. R., and Lockard, D. P., "Effects of Geometric Details on Slat Noise Generation and Propagation," *International Journal of Aeroacoustics*, Vol. 9, No. 4-5, 2010, pp. 655–678. doi:10.1260/1475-472X.9.4-5.655.

[22] Fares, E., Casalino, D., Ribeiro, A., Choudhari, M., and Lockard, D. P., "PowerFlow Simulations of the Aeroacoustics of 30P30N Multi-Element Airfoil," *Proceedings of AIAA BANC-III Workshop*, Atlanta, GA, 2014.

[23] Pascioni, K., "An Aeroacoustic Characterization of a Multi-Element High-Lift Airfoil," Ph.D. thesis, Florida State University, Tallahassee, FL, 2017.

[24] Anderson, J., *Fundamentals of Aerodynamics*, 5th ed., McGraw-Hill Education, 2010.

[25] Reger, R., Zawodny, N., Pascioni, K., Wetzel, D., Liu, F., and Cattafesta, L., "Design-optimization of a broadband phased microphone array for aeroacoustic applications," *Journal of the Acoustical Society of America*, Vol. 131, 2012.

[26] Scholten, W., Patterson, R., Eustice, M., Cook, S., Hartl, D., Strganac, T., and Turner, T., "Aerodynamic and Structural Evaluation of an SMA Slat-Cove Filler Using Computational and Experimental Tools at Model Scale," *ASME 2018 Conference on Smart Matl., Adaptive Struct. and Intell. Sys., SMASIS 2018-8129*, San Antonio, TX, 2018. Submitted.

[27] Turner, T. L., and Long, D. L., "Development of a SMA-Based, Slat-Gap Filler for Airframe Noise Reduction," *23rd AIAA/AHS Adaptive Structures Conference*, American Institute of Aeronautics and Astronautics, Reston, Virginia, 2015. AIAA paper 2015-0730.